Keeping it simple: Fabrication of three-layered, purely quantum dot-based light-emitting electrochemical cells

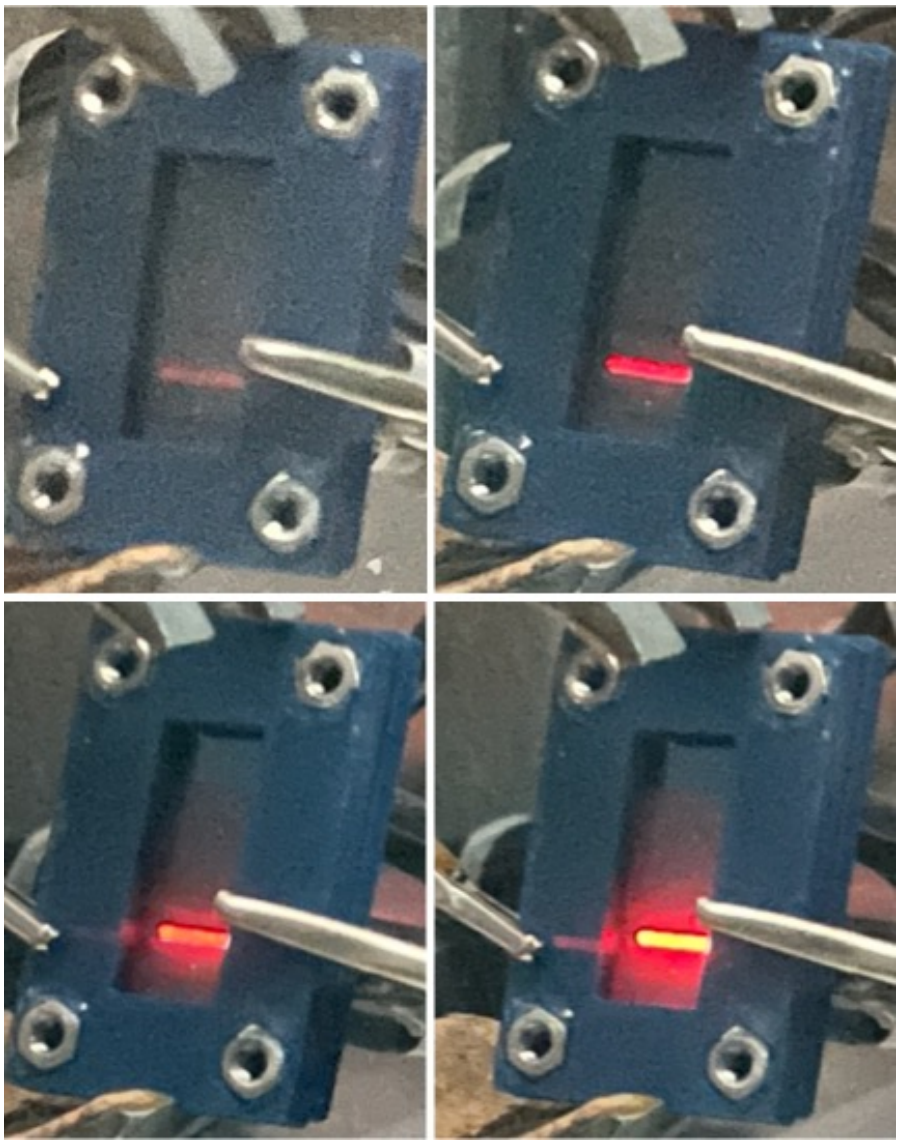

TU Delft

Delft University of Technology

KEEPING IT SIMPLE:
FABRICATION OF THREE-LAYERED, PURELY QUANTUM DOT-BASED LIGHT-EMITTING ELECTROCHEMICAL CELLS

By

Jesse ‘t Hoen

In partial fulfillment of the requirements for the degree of

Master of Science
In Chemical Engineering

At the Delft University of Technology
Faculty of Applied Science
Opto-electronic Materials
Department of Chemical Engineering

To be defended publicly on Thursday 31st of March 2022 at 13:00 PM

Supervisor:	prof. dr. A.J. Houtepen
Daily supervisor:	R.F. Ubbink
2nd Examiner:	dr. T.J. Savenije
3rd Examiner:	dr. D.A. Vermaas

March 2022

Beverwijk

Preface

Thank you for reading this section. This document entails my master thesis project, one of the final hurdles before completing the master program of Chemical Engineering at the TU Delft.

In this thesis I will show that it is possible to construct and operate a three-layered light-emitting electrochemical cell (LEC) that holds quantum dots (QDs) as its only emissive species. This is something that, to the best of my knowledge, has not been shown in the scientific world before.
When I had the first meeting about this project together with Arjan and Reinout in May 2021, Arjan told me that it would be fantastic if I succeeded in getting this device structure to work within his research group. That I now, ten months later, have not only been able to do so, but can also call myself a pioneer in the field of QD-based LECs, makes me extremely proud.

The great results that I managed to acquire would not have been possible without the help of Arjan and especially Reinout.
Arjan, I want to thank you for all the in-depth discussions we have had. You have taught me to be critical at the results you gather like no one else can and to sometimes take a few steps back before you proceed. Next to this, you made me realize that it is not a bad thing to not understand everything. On the contrary, this is what makes research so much fun. Your lessons have made me a better scientist and I am grateful for that.
Reinout, what a journey this has been. Building forth on your own master thesis project, I was the first student you had to supervise as a PhD candidate. I think it is safe to say that we have learned a lot from each other and had a lot of fun while doing so. It still buzzes me how much knowledge you possess, and not only on our project. You have been a great supervisor to me who always helped me when I needed it. I know I can be quite demanding and that I can be a pain in the ass from time to time. Your calm character and analytic view on the obstacles we had to overcome is something I really liked. I want to thank you for everything you have done for me, and I wish you all the best in the three years to come in this research group.

Next to Reinout and Arjan, I want to express my gratitude towards the whole NCFun group. This group is really a fun group and I have been walking around with a smile on my face for about six months, day in day out. I want to thank everyone for their fruitful insights, lovely lunch breaks and enjoyable journal club sessions. I wish everyone the best of luck in their projects and further careers.

After this master thesis project, I will leave the scientific world behind me (but perhaps only temporarily). I will pursue a Double Degree in Chemical Engineering and Management of Technology. This master thesis marks the end of the first part of this journey. The second part has already started alongside the final stage of this master thesis. This has put a lot of weight on my shoulders in the last two months of this project but has shown me that my discipline and perseverance are stronger than they have ever been. I am looking forward to the path that lies in front of me.

If there is one lesson that I have learned during this thesis that I want to pass on to anyone reading this thesis, it would be the following: you cannot fail if you do not stop trying.
This project has faced me with a lot of setbacks and demotivating moments, but I have always found the drive to keep pushing on, to just try again. This is a lesson that has shaped me to a better version of myself and this is what I am most thankful for.

Jesse ‘t Hoen
Beverwijk, March 2022

Abstract

Light-emitting electrochemical cells (LECs) form a cheap and easily produced alternative to (organic) light-emitting diodes ((O)LEDs) due to their simple device structure and the ability to form an *in-situ* p-i-n junction. Usage of quantum dots (QDs) as a luminophore in LECs is expected to result in devices with improved emission properties and stability compared to polymer-based LECs. LECs that use QDs as their only luminophore have, however, not been operated successfully without the presence of additional charge carrier injection layers and/or the inclusion of polyvinylcarbazole (PVK) as host (and light-emitting) polymer, yet. In this thesis, I show that three-layered, purely QD-based LECs can be fabricated and operated fruitfully. A crucial step to achieving this was carrying out a ligand exchange (LE) on the QDs, replacing the long aliphatic ligands that passivate the QD surface with short BF_4^- ions and thereby improving the conductivity of the QD film. LECs were then produced using the ligand exchanged QDs, both with and without additional charge carrier injection layers. The three resulting devices were confirmed to operate as LECs and show light emission at positive bias. The current density and electroluminescence (EL) intensity increase as the applied bias is increased for all three the LECs. The three types of LECs were compared on their electrical response and emission. Turn-on voltages and stability windows were also determined for the three types of devices. Improvement of LEC performance is suggested to be achieved by enhancing the photoluminescent quantum yield (PLQY) of the QDs, excluding side reactions that might take place in the LEC under operation or optimizing the current device structure.

Keywords: Light-emitting electrochemical cell, colloidal quantum dots, ligand exchange, electroluminescence

Table of contents

List of abbreviations

Å	Angstrom
ACN	acetonitrile
Al	aluminum
BuOH	1-butanol
CdO	cadmium oxide
CdS	cadmium sulfide
CdSe	cadmium selenide
cm	centimeter
CV	cyclic voltammetry
DMF	N,N-dimethylformamide
ECDM	electrochemical doping model
EDL	electronic double layer
EDM	electrodynamic model
EL	electroluminescence
EQE	external quantum efficiency
ETL	electron transport layer
EtOH	ethanol
EU	European Union
eV	electron volt
FTIR	Fourier transform infrared
g	gram
HCl	hydrochloric acid
HF	hydrogen fluoride
HOMO	highest occupied molecular orbital
HTL	hole transport layer
HWHM	half width at half maximum
InP	indium phosphide
IPA	1-propanol
iTMC	ionic transition metal complex
ITO	indium tin oxide
KOH	potassium hydroxide
LE	ligand exchange
LEC	light-emitting electrochemical cell
LED	light-emitting diode
$LiCF_3SO_3$	lithium trifluoromethanesulfonate
lm	lumen
LUMO	lowest unoccupied molecular orbital
M	molar
mA	milliampere
mbar	millibar
MEH-PPV	poly[2-methoxy-5-(2-ethylhexyloxy)-1,4-phenylenevinylene]
MeOH	methanol
mg	milligram
MHz	megahertz
mL	milliliter
mm	millimeter
nm	nanometer
NMR	nuclear magnetic resonance
$NOBF_4$	nitrosonium tetrafluoroborate
OA	oleic acid
ODA	octadecylamine
ODE	1-octadecene
OLAM	oleylamine
OLED	organic light-emitting diode
PA	propionic acid
PEDOT:PSS	poly(3,4-ethylenedioxythiophene):polystyrenesulfonat
PEO	poly(ethylene oxide)
PL	photoluminescence
PLQY	photoluminescent quantum yield
ppm	parts per million
PVK	polyvinylcarbazole
QD	quantum dot
RPM	rounds per minute
S	sulfur
s	second
Se	selenium
T	temperature
TEM	transmission electron microscopy
TOP	tri-n-octylphosphine
TOPO	tri-n-octylphosphine oxide
$triBF_4$	triethyloxonium tetrafluoroborate
UV	ultra-violette
V	volt
W	watt
ZnO	zinc oxide
ZnS	zinc sulfide
µL	microliter

Introduction

As of 2021, a little under 20% of the worldwide electricity consumption can be attributed to lighting applications.[1-3] It therefore comes as no surprise that there is an ever-lasting, global desire to optimize the performance of lighting applications ever since the rise of the first incandescent lightbulb around 1860.[2]

Even in 1965, after almost a hundred years of incremental improvements, incandescent lightbulbs still converted 95% of the incoming power into heat. The first notable step forward arose in the form of fluorescent lamps. Their efficiency increased fourfold when compared to incandescent lighting sources.[2]

The successor of the fluorescent lamp, the light-emitting diode (LED), arose around 1960 and is actually the most used lighting source nowadays.[2] In LEDs, light emission is achieved via electroluminescence (EL). This is achieved by sandwiching a luminophore between two electrodes. When a bias is applied over the electrodes, electrons and holes are injected into the device and recombine within the luminophore, resulting in the emission of photons.
Trying to improve LEDs further, Kido et al. fabricated the first LED with an organic emissive layer (OLED) in 1993.[5] By swapping the inorganic emissive layer for an organic one, the LEDs become thinner and more flexible,[6] opening up the way for flexible displays. Ultramodern OLEDs nowadays progressed towards lifetimes of over 10,000 hours,[7] with power efficiencies nearing 200 lm W^{-1} as claimed by companies like Cree LED[8] and Philips[9] and an external quantum efficiency (EQE) exceeding 80%.[10] A schematic of the device structure of a state of the art OLED and the corresponding energy levels is shown in **Figure 1A**.

Ideally, the work function of the cathode is low and matches the energy level of the conduction band of the light-emitting species, while the work function of the anode is high and matches the energy level of its valence band.[4] In this way, electrons and holes can be injected into the conduction band and valence band of the luminophore, respectively.

In reality, a mismatch of work functions between the electrodes and the HOMO and LUMO of the luminophore results in barriers for charge carrier injection. To overcome these barriers, additional layers for charge carrier injection as well as charge carrier transport are needed. The materials these layers are made of need to be chosen carefully, as their fermi levels need to lie between the energy level of the valence band and the anode and between the energy level of the conduction band and the cathode. The extra layers complicate the device structure of (O)LEDs drastically.

Deduced from the above, OLEDs show great potential of becoming the standard for lighting applications. Their cost of production is, however, still rather high,[11] hampering their potential for large-scale diffusion as described by Ortt and Schoormans.[12] The noteworthy cost of production is mainly due to their complicated buildup.

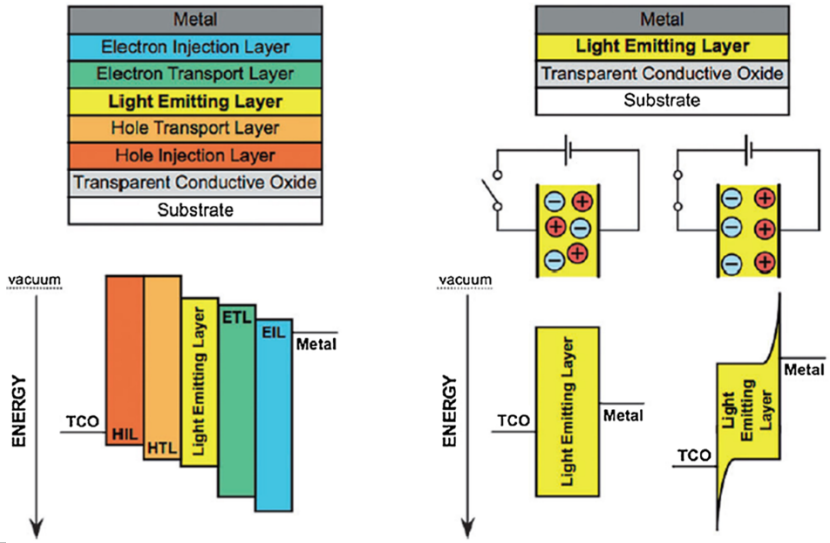

Figure 1. (A) Schematic overview of a common buildup of an ultramodern OLED and the accompanying energy levels. **(B)** Schematic overview of a common buildup of an ultramodern LEC and the accompanying energy levels. An electric field is developed since charged dopants are created when electrons or holes start flowing, resulting in a so-called Schottky barrier. The EDL that forms as a result makes the electrostatic potential that the charge carriers experience differ with their position, resulting in the bending of the energy levels of the valence and conduction band. The simplification of the device structure when going from a LED to a LEC is clearly visible. Reprinted from [4].

In order to simplify the complicated device structure of (O)LEDs, the light-emitting electrochemical cell (LEC) emerged in 1995.[13] In LECs, the barriers for charge carrier injection are not overcome by a number of supplementary layers, but through the addition of solid electrolyte containing mobile ions. The mobile ions form an electronic double layer (EDL) at the electrode-active layer interface when a bias is applied over the electrodes. They also participate in the formation of an *in-situ* p-i-n junction when the device becomes electrochemically doped. A schematic of the device structure of a typical LEC and the corresponding energy levels are shown in **Figure 1B**.

LECs have been produced with lifetimes of 2,700 hours,[14] power efficiencies of 83.4 lm W^{-1} and an EQE of 35.4%.[15]
These numbers show that the absolute performance of LECs is still inferior to that of OLEDs. This is currently the bottleneck for the large-scale diffusion of LECs, despite their more cost friendly nature when compared to (O)LEDs. **Figure 2** clearly shows that the scientific interest in (and therefore the development of) LECs is still in its infancy upon comparison with LEDs. It could therefore be possible that LECs will replace LEDs as the number one lighting source in the future.

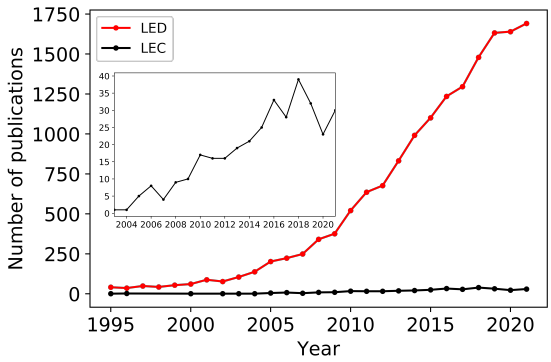

Figure 2. Number of publications that include the terms 'Light-emitting diode' and 'Light-emitting electrochemical cell' in their abstract during the past 27 years. The inset shows an amplification of the last nineteen years of the LEC curve and visualizes an increasing interest in LECs (source: Pubmed).

Several materials have been used as luminophores in the active layer of LECs. Examples are light-emitting polymers[13, 16, 17] and ionic transition metal complexes (iTMCs).[18-20]
To the best of my knowledge, the incorporation of quantum dots (QDs) as only luminophore in LECs has not led to successful fabrication of the simple, three-layered device structure as depicted in **Figure 1A**, yet.[21-26] The studies that have come closest to this simple structure always incorporated a hole injection layer and/or used polyvinylcarbazole (PVK), a light-emitting polymer, as host polymer.
I hypothesize that in principle, the simple, three-layered device structure of a LEC should be able to be constructed with any luminophore. With this thesis, I show that it is possible to fertilely build and operate a three-layered, purely QD-based LEC without the need of a hole injection layer and/or PVK as host polymer. This result hints that this hypothesis might very well hold true. I also indicate what factors are found to be crucial for fruitful device fabrication and operation.

To comprehend this thesis, some theoretical background information concerning semiconductors, QDs and QD-based devices will first be given in the first chapter.
Hereafter, LECs will be fabricated in chapter two, and their performance validated in chapter three.
Finally, ideas for future device construction are given in chapter four.

1. Theoretical background

This chapter gives all the relevant theoretical background information needed to comprehend this thesis. Some of the concepts are common knowledge. Still, I think it is beneficial to have a structured, in-depth overview of all the theories and concepts.

1.1 Metals, semiconductors, and insulators

The theories behind solids are rather complicated and still not fully understood. Literature on this topic is widely available but often hard to comprehend. The upcoming explanation of metals, semiconductors, and insulators (and how their differences arise) is meant to be relatively simple. The concepts in sections **1.1.1 The Pauli-Sommerfeld theory** and **1.1.2 The zone theory of solids** are extracted from a paper written by Seitz and Johnson.[27] For more in-depth theories the reader is referred to books concerning the theory of solids. An example is [28]. It provides more depth but roughly draws roughly the same conclusion as Seitz and Johnson.

1.1.1 The Pauli-Sommerfeld theory

The first class of solids, metals, are materials that can conduct electricity and heat and are tough and durable. The Pauli-Sommerfeld theory of metals is needed to understand the energy landscape of metals.
The theory arose after the discovery of quantum mechanics for atomic systems. Pauli stated that the valence electrons in the whole metal are free to move. Their energy, E, is given by:

$$\boxed{E - V_0 = \frac{p^2}{2m}} \qquad (1)$$

where m is the mass of the electron, p its momentum and V_0 the potential energy, which is assumed to be uniform throughout the metal. In line with the rules of quantum mechanics for atomic systems, the vector momentum cannot obtain all values. Only the ones that satisfy the following relations for p_x, p_y and p_z are allowed:

$$\boxed{p_x = \frac{n_x \hbar}{L_x}}, \boxed{p_y = \frac{n_y \hbar}{L_y}}, \boxed{p_z = \frac{n_z \hbar}{L_z}} \qquad (2)$$

where $\hbar$ is Planck's constant over 2π, L_x, L_y and L_z are the length, width, and height of the crystal sample and n_x, n_y, and n_z are integers. These criteria yield quantified energy levels instead of continuous ones for a finite crystal. The number of energy states scales with n and is extremely large for crystals of ordinary size. Each state has its own unique energy level but since there are so many states the energy spectrum can be seen as continuous.
Then, Pauli remarked that each energy state can contain at most two electrons: one with its spin factor in positive direction and one with its spin factor in negative direction. In this way the magnetic moment within the crystal balances out to zero. This phenomenon is called the Pauli exclusion principle. Due to this principle, the electrons will only fill half of the available states at T=0 Kelvin. The energy level of the highest occupied state at T=0 Kelvin is called the Fermi level. The valence electrons can easily be excited to higher, unoccupied energy states by for instance thermal excitation. It is mostly the valence electrons that can be excited, since deeper lying electrons cannot move to higher energy states as these are already filled. A schematic overview of the energy distribution of a metal is shown in **Figure 1.1.1.1**.

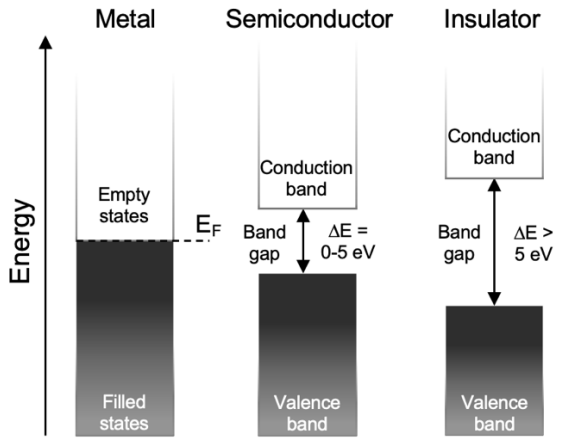

Figure 1.1.1.1. Band structures of (*left*) metals, (*center*) semiconductors, and (*right*) insulators. The Fermi level in metals is indicated as E_F. Semiconductors have band gaps between 0 and 5 eV, while insulators have band gaps larger than 5 eV.

1.1.2 The zone theory of solids

The difference between metals and insulators and semiconductors is not obvious from the Pauli-Sommerfeld theory. To concretize this difference another theory is needed: the zone theory of solids.
This theory adds the periodic potential distribution within a solid lattice and the wave character of the electron to the previous theory.

The outcomes of the Schrödinger equation for an electron that moves in a solid crystal are described by the wave number vector. It is

symbolized as σ and has a magnitude of λ^{-1} where λ is the De Broglie wavelength (λ = h/p) of the wave associated with a particle that moves with a certain momentum. If an electron moves with a constant total energy E and moves within a constant potential field V_0, as is the case in the Pauli-Sommerfeld theory, then:

$$E - V_0 = \frac{p^2}{2m} = \frac{h^2}{2m\lambda^2} = \frac{h^2\sigma^2}{2m} \qquad (3)$$

and the energy thus scales quadratically with σ. This is visualized in **Figure 1.1.2.1A**.

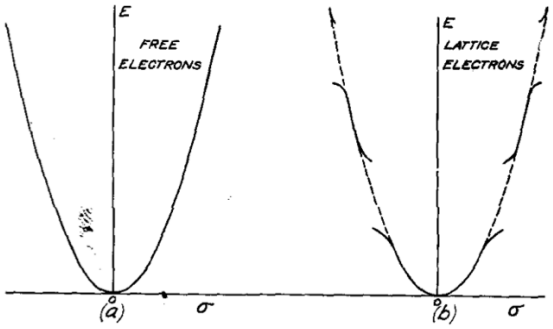

Figure 1.1.2.1. (A) Quadratic dependence of energy E on wave vector σ for an electron in a uniform, one-dimensional potential field. **(B)** Non-quadratic dependence of E on σ for an electron in a periodic, one-dimensional potential field. Reprinted from [27].

The potential field the electron experiences in a real solid, however, is not the same everywhere in the crystal. The potential field is position dependent and is influenced by several parameters. Luckily, it is obvious that the average potential field must be periodic since the crystal is simply a repetition of its unit cell.

It is found that the energy of an electron in such a periodic potential field does not scale with σ quadratically but depends on the magnitude as well as on the direction and the configuration of σ. The generic form of E(σ) is shown in **Figure 1.1.2.1B** for a given direction of σ.

Discontinuities arise for particular values of σ – forbidden energy states of the electron become apparent, just as predicted by the Pauli-Sommerfeld theory. Sometimes a disallowed energy range for one direction of σ is overlapped by an allowed energy range for another direction of σ. This is envisaged in **Figure 1.1.2.2A.** This leads to a continuous energy spectrum for metals and this phenomenon is also in line with what is found from the Pauli-Sommerfeld theory.

For semiconductors and insulators, the energy ranges for different directions of σ do not fully overlap, leading to a large energy gap where an electron is not allowed to be in, no matter its momentum. This energy gap is known as the bandgap and is visualized in **Figure 1.1.2.2B**. The discrepancy between insulators and semiconductors is the size of this bandgap. For semiconductors the bandgap is typically 0-5 eV, while the bandgap for insulators is larger than 5 eV. The continuous energy bands below the bandgap are bundled as the valence band, while the continuous energy bands above the bandgap are called the conduction band. A schematic of insulators and semiconductors and their energy distributions is shown in **Figure 1.1.1.1**.

The most used semiconductor is crystalline silicon.[29] Semiconductors can, however, also be constructed by combining equimolar quantities of group Ⅲ and group V elements, or even from elements of group Ⅱ and Ⅵ. Half of the entities have one/two valence electrons in surplus, while the other half of the atoms have a one/two valence electron deficit. The addition of the two different materials results in charge neutrality.

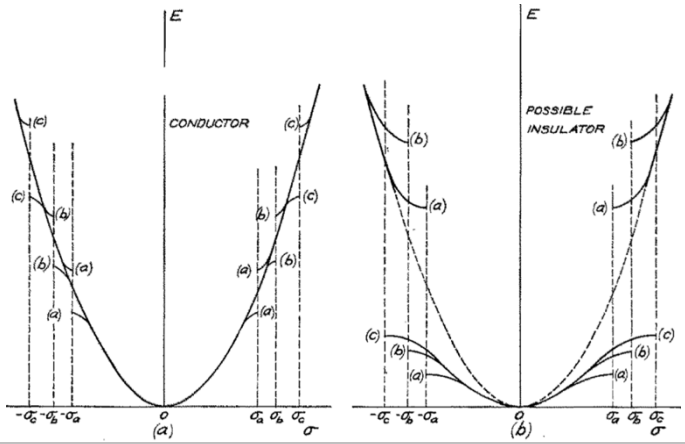

Figure 1.1.2.2. (A) Dependence of E on σ for three directions of σ. Energy gaps exist at ± σ_a, ± σ_b, ± σ_c while the allowed ranges overlap, resulting in no forbidden energy states and thus a continuous energy landscape for metals. **(B)** The band gap for insulators and semiconductors arises since the energy gaps are so wide that complete overlap of the allowed ranges is not possible. Reprinted from [27].

The size of the bandgap of bulk semiconductors is influenced by the materials picked for their construction.

1.1.3 Electron/hole recombination in semiconductors

In the intrinsic state, the conduction band of a semiconductor is empty barring a small population of thermally excited electrons. The opposite is true for the valence band, which is almost entirely filled up by electrons. The small number of electrons in the conduction band and holes in the valence band result in the ability of a semiconductor to conduct tiny amounts of electricity, hence the term semiconductor. Additional electrons can, however, be excited from the valence band to the conduction band. This can be done by i.e. thermal excitation or by the adsorption of a photon, as long as the energy supplied is equal to or larger than the bandgap. When an electron leaves the valence band, it leaves behind a positive charge since charge neutrality must be maintained. This 'void' is called a hole. Holes are mobile species, too. Electrons in the vicinity of the hole can move into the hole, effectively transporting the hole.
After the electron is excited to the conduction band, it can fall back to the valence band and recombine with the positively charged hole. Both species are simultaneously annihilated by this process which is referred to as (electron-hole) recombination. There are three ways the electron and hole can recombine:[30] radiative, Auger, and defect level driven. The three types of recombination are illustrated in **Figure 1.1.3.1**.

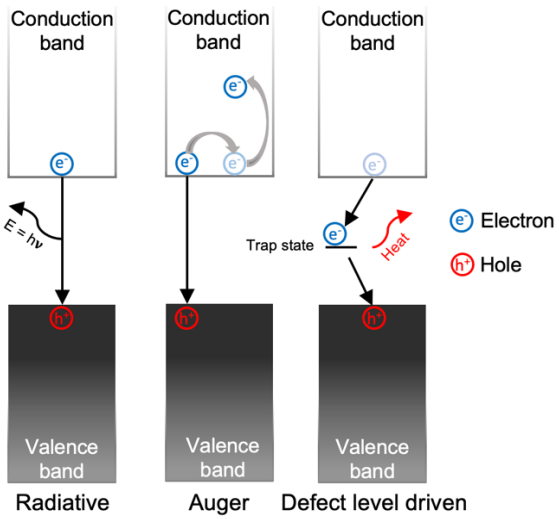

Figure 1.1.3.1. The three types of recombination. A photon with energy equal to the width of the band gap is released in radiative recombination (*left*). For Auger recombination, the electron passes its energy to an adjacent electron to promote it further into the conduction band (*center*). For Shockley-Read-Hall recombination, the electron first travels to a so-called trap state before it releases its energy in the form of heat when falling back to the valence band (*right*).

In defect level driven recombination, also known as Shockley-Read-Hall recombination,[30] interstitials, impurities or vacancies in the lattice introduce energy states within the bandgap. In a multi-step process, the energy is released non-radiatively in the form of thermal vibrations via these trap states. These thermal vibrations are called phonons and are adsorbed by the lattice, resulting in heating of the lattice.
For almost all lighting applications radiative recombination is the intended process. Defect level driven recombination and Auger recombination compete with this process and are thus unwanted. Interstitials, vacancies, and impurities must therefore be avoided as much as possible.

1.1.4 Doping in semiconductors

Some of the atoms in crystalline semiconductors can be replaced by other atoms. If the replacing atoms have a differing number of valence electrons, they can either donate electrons into the conduction band or withdraw electrons from the valence band (add holes to the valence band). This process is referred to as chemical doping. Although it was not exactly named like this, the phenomenon was first described in 1950 in a patent issued by John Robert Woodyard.[31]
Doping affects the Fermi level of semiconductors. In intrinsic silicon at T=0 Kelvin, the Fermi level lies exactly between the valence band and conduction band. Adding electrons to the conduction band is called n-type doping as there are more mobile negative species in this scenario. This type of doping shifts the Fermi level upwards. Adding holes to the valence band is called p-type doping, as there are more mobile positive species here. In this case, the Fermi level shifts downwards.
If the magnitude of doping is above a certain threshold, semiconductors can behave like metallic conductors.
Next to chemical doping, semiconductors can also be doped electrochemically. Here, electrons and/or holes are injected into the semiconductor from an outside source. This process is essential to the functioning of LECs and will be explained later in this thesis.

1.1.5 p-n junctions in semiconductors

A phenomenon that can occur when dealing with doping is that of the formation of a p-n junction. When one side of the semiconductor is p-doped and the other side is n-doped, the excess electrons and holes can recombine at

the regime where the doped zones meet. This recombination regime between the zones that are p-type doped and n-type doped is called a p-n junction.[32] The formed p-n junction is the result of an equilibrium between two forces acting on the charge carriers: a diffusional force and an electrostatic force.
The first force results in the diffusion of charge carriers to the opposite doped region where the concentration of this charge carrier is lowest. Holes flow to the n-type doped region, while electrons flow to the p-type doped zone.
The latter force is more complicated. In the p-type doped region holes are the *majority carrier*, while electrons are the *minority carrier*. The reverse holds for the n-type doped region. When a hole moves towards the n-type region due to the diffusional force, it becomes the minority carrier. Because of this, the hole will have a short lifetime and will recombine with one of the electrons very quickly. In the p-type region, however, the hole has left behind a static negative charge. Due to this, a small zone of the p-doped region near the interface becomes negatively charged. For the n-doped region the opposite is true. The result of the accumulation of all the static dopants is the rise of an internal electric field. This electric field exerts an electric force on the holes, pulling them back to the p-type doped region. For the electrons, the opposite holds.
The diffusional force and the electric force operate in opposite directions for the charge carriers. Their equilibrium creates the p-n junction, which is referred to as the space charge region since there is buildup of net charge. The creation of a p-n junction is schematically shown in **Figure 1.1.5.1**.

When a bias is applied over a material and the n-type region is connected to the negative side of this bias and the p-type region is connected to the positive side of the bias, a forward bias is applied. Electrons can flow through the n-type region to the p-n junction and holes can do this through the p-type region. In this way, recombination of the two charge carriers will happen continuously. If the recombination is radiative, light will be emitted from the p-n junction under forward bias.

1.1.6 Semiconductor-metal contacts

Semiconductor-metal contacts are important to ensure good performance in many semiconductor devices. The upcoming theory is extracted from chapter 10 of the book called 'Semiconductor Physical Electronics'.[28]
There are two types of semiconductor-metal contacts: Ohmic contacts and Schottky contacts. While Ohmic contacts show a linear (non-rectifying) current-voltage (I-V) response, Schottky contacts show a non-linear (rectifying) I-V response.
Two cases can arise when considering semiconductor-metal contacts: one where the Fermi level of the semiconductor lies higher than the Fermi level of the metal and one where the Fermi level of the semiconductor lies below the Fermi level of the metal.
In the first case, the work function of the metal, the energy needed to promote an electron from the surface (or the Fermi level) of the material into the vacuum, is larger than the work function of the semiconductor. Before intimate contact between the two materials is

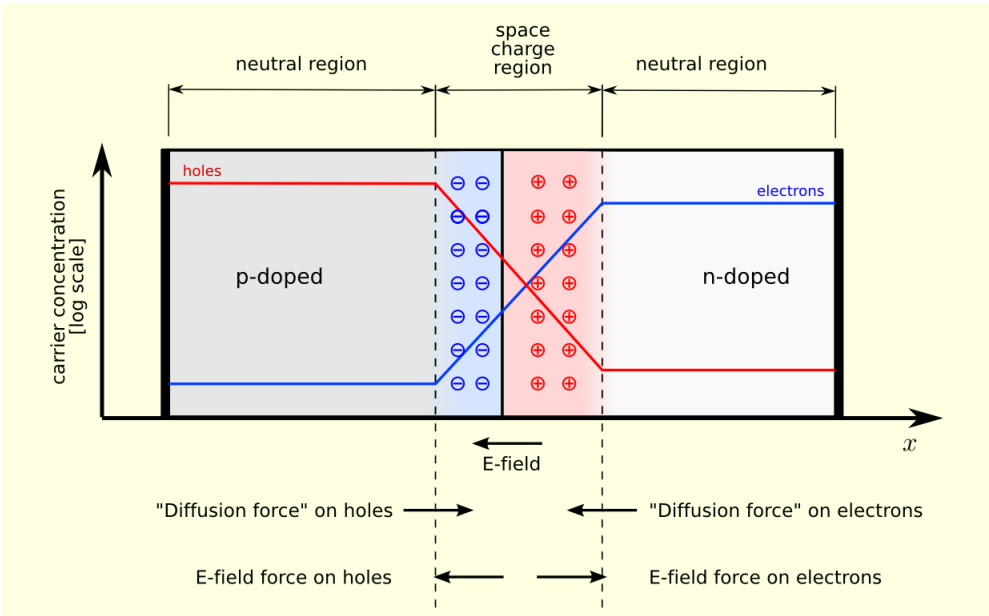

Figure 1.1.5.1. A p-n junction at an applied bias of zero volt at thermal equilibrium. The blue line and the red line show the electron and hole concentration, respectively. The blue region is negatively charged while the red region is positively charged. The grey regions are charge neutral. The acting forces are shown at the bottom of the figure and indicate a diffusional force and a drift force. The space charge region originates from an equilibrium between these two forces. Reprinted from [33].

established, the energy diagram looks as shown in **Figure 1.1.6.1A**. Then, when intimate contact is established, the electrons in the semiconductor can lower their energy by flowing out of the semiconductor and into the metal. This happens until the Fermi levels of the metal and semiconductor are aligned. The shifted electrons leave behind positive, static dopants that create an internal electric field. This field results in the bending of the edges of the energy levels of the conduction band, valence band and vacuum energy level. The electrons now experience a position dependent electrostatic potential. This process is known as the image-lowering effect, or Schottky, effect. The result is an energy barrier for electron transfer, the Schottky barrier, which is equal to the difference between the work function of the metal and the electron affinity of the semiconductor. The presence of Schottky barriers in a semiconductor-based device can greatly hamper its electrical conductivity and thus its performance. The formation of the Schottky barrier is shown in **Figure 1.1.6.1B**.

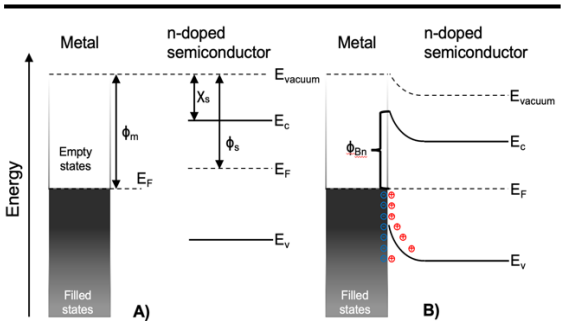

Figure 1.1.6.1. Creation of a Schottky contact. φ_m is the work function of the metal and φ_s is the work function of the semiconductor. χ_s is the electron affinity of the semiconductor. φ_{Bn} is the Schottky barrier. **(A)** Before intimate contact is established. **(B)** After intimate contact is established. Red dots are static positive charges and blue dots are the moved electrons. The image-lowering effect is well visible. The rise of the finite Schottky barrier leads to rectifying behavior.

In the second case, the work function of the metal is lower than the work function of the semiconductor. The energy diagram before intimate contact is shown in **Figure 1.1.6.2A**. After intimate contact is established, the electrons can lose energy if they flow from the metal into the semiconductor. Although the edges of the energy bands are also bended here, the Schottky barrier is not formed. This can be seen in **Figure 1.1.6.2B** and the created contact is known as an Ohmic contact. In Ohmic contacts the electrons can easily travel back and forth between the semiconductor and metal. This explains the non-rectifying behavior and the symmetric I-V response. The voltage drop across the interface is negligible and the resistance of the material adheres to Ohms law: U = I * R.

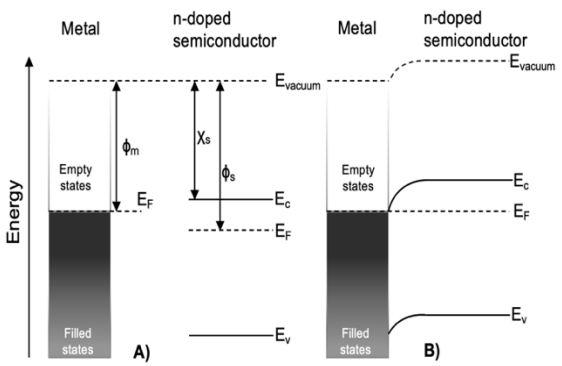

Figure 1.1.6.2. Creation of an Ohmic contact. φ_m is the work function of the metal and φ_s is the work function of the semiconductor. χ_s is the electron affinity of the semiconductor. **(A)** Before intimate contact is established. **(B)** After intimate contact is established. The absence of the Schottky barrier leads to the non-rectifying behavior.

For p-type doped semiconductors (and thus for holes) the opposite relationship between the work functions of the metal and the semiconductor and the type of contact formed holds true.
Selection of proper contact materials is pivotal in ensuring charge carriers can move into, through and out of semiconductor materials effectively.

1.2 Quantum dots

As discussed in section **1.1 Metals, semiconductors, and insulators**, bulk semiconductors show very sharp and well-defined continuous bands above and below the bandgap. If, however, the dimensions of a semiconductor are scaled down to nanometer sizes, the edges of the bands become discontinuous. The width of the bandgap is no longer solely a material property but also depends on the shape and size of the crystal. This is visualized in **Figure 1.2.1**.

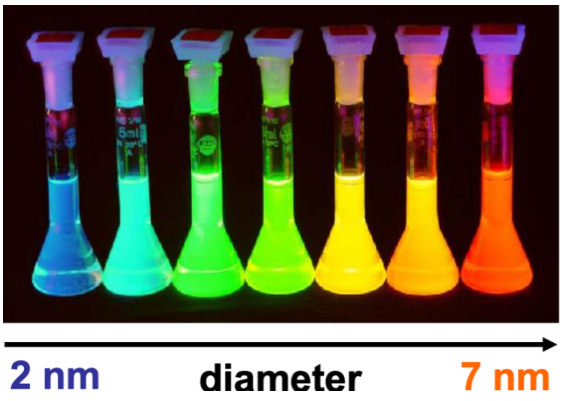

Figure 1.2.1. Semiconductor nanocrystals of the same material, CdSe. Due to the difference in size, different band gap widths are established which is visualized by the emission of photons of different wavelengths. Reprinted from [34].

This means that luminophores emitting different colors can be created simply by growing crystals of different sizes of the same materials. In other words, it is possible to specifically engineer the emission wavelength of these semiconductor nanocrystals. This property in combination with their sharp emission linewidths has attracted a lot of attention, as it allows for the construction of displays with a very wide color gamut. Additionally, the nanocrystals could find application in other types of lighting devices such as LEDs or lasers.

As predicted by the Pauli-Sommerfeld theory, an extremely large number of energy states is available in a semiconductor crystal of ordinary size. Although each energy state has its own unique energy level, the difference in energy between states is so small that a continuous energy band appears above and below the bandgap. When the dimensions of the crystal are scaled down to the nanometer scale, however, the electrons within the crystal are confined to a tremendously smaller volume. When the crystal becomes so small that the dimensions of it are of the same order of magnitude as the de Broglie wavelength of the electrons within that crystal, the quantum confinement effect comes into play. The more confined (the smaller the crystal) the electrons are, the wider the spacing between succeeding energy levels becomes. This leads to enlargement of the width of the band gap as well as the creation of distinct energy levels at the edges of the band gap. Since the energy levels at the band edges are now so well-separated, very distinct adsorption and emission energies (and thus wavelengths) become apparent. This is envisioned in **Figure 1.2.2**. For a more thorough understanding of the quantum confinement effect the reader is referred to the particle-in-a-box model.

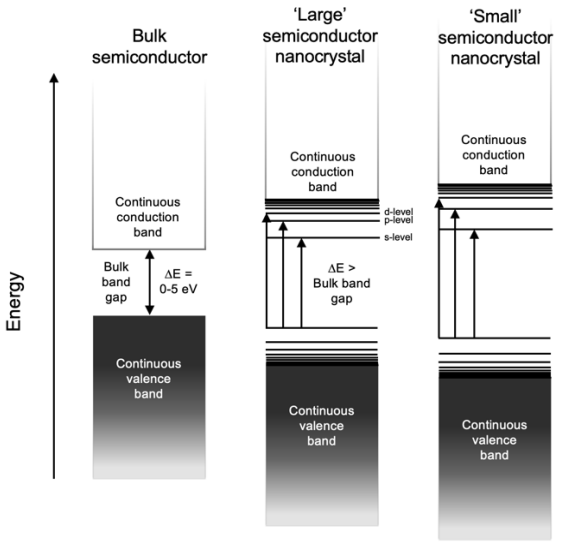

Figure 1.2.2. The band structures of bulk semiconductors (*left*) as well as nanocrystal semiconductors of two sizes (*center and right*). Where the bulk semiconductor has a sharp, well-defined band edge, the nanocrystals show distinct energy levels at the band edges. The absolute width of the band gap as well as the width of succeeding energy levels increases as the crystal size decreases. Therefore, distinct energy transitions can become apparent, which are visualized with the arrows.

The nanocrystals of semiconductors are commonly known as (colloidal) quantum dots (QDs). They can be synthesized in ensembles and in solution through various methods,[35] like reduction, thermal decomposition methods and nonhydrolytic sol-gel methods. Ideally, all nanocrystals are of the same size, resulting in an energy landscape that is the same for each QD. The radiative recombination of electrons when they fall back from the 1S-level to the valence band would result in the emission of photons that all have the same wavelength. However, the adsorption and emission peaks

of an ensemble of QDs always have a non-zero width. The more monodisperse the particles are, the narrower these peaks are. Narrow emission peaks translate to monochromatic photon emission, something that is often desired in device fabrication.

After their synthesis, QDs are inherently unstable, as they contain many reactive surface atoms. The surface can be protected by passivating ligands that are retained on the surface of the QDs during their synthesis.[36] Besides passivating the surface, the ligands also solubilize the QDs in dispersions. By picking appropriate ligands, stable colloidal dispersions of QDs in (a)polar solvents can be prepared. These dispersions can then be processed through several cheap, large area liquid-based deposition techniques, such as spin coating, drop casting and inkjet printing.[37]

Although ligands can passivate most of the surface states, some remain. These residual dangling orbitals can result in trap states that deteriorate the performance of the QDs. Their photoluminescence quantum yield (PLQY), the number of photons emitted per excited electron, can drastically deviate from unity because of these trap states. Optimizing the surface coverage of the QDs by the ligands can increase the PLQY. Growing a shell (or multiple) of a wider bandgap material around the semiconductor core to passivate the trap states can also result in extremely stable QDs with PLQYs nearing 100%.[39-41]

1.2.1 Doping of QD films

In analogy to what has been discussed in section **1.1.4. Doping in semiconductors**, QDs can also be doped via lattice substitution. Unfortunately, the interstitials included to achieve this doping can also induce the formation of trap states.[42] The dopants create extra states that can end up in the bandgap. Recombination via these trap states can compete with radiative recombination, lowering the PLQY.
Beside doping with impurities, QDs can also be doped in other ways. Examples of alternative manners of doping are redox injection[43, 44] and photodoping.[45, 46]
In the first, electrons are supplied via other compounds through a redox reaction. In the latter, a hole is created via photoexcitation of an electron, whereafter the hole can transport to surrounding QDs.
A third approach to dope QDs is that of electrochemical doping.[47] The QDs can be loaded into an electrochemical cell together with an electrolyte. A QD film is deposited on a working electrode, which is then placed in an electrolyte while a counter electrode is placed in the same solution. Electrons/holes can be injected into the QD layer depending on whether the applied voltage to the working electrode is negative/positive. To compensate the excess charges, the mobile ions of opposite charge of the electrolyte will diffuse into the QD film as much as possible. This process is schematically shown in **Figure 1.2.1.1**.

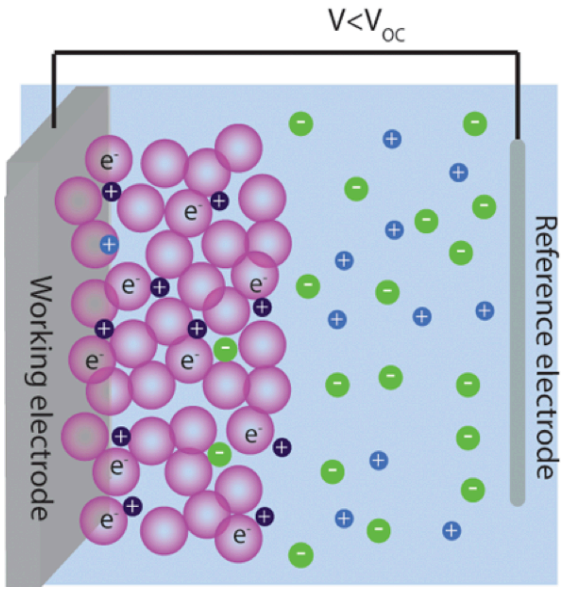

Figure 1.2.1.1. Schematic overview of electrochemical doping of a thin QD film. Whilst electrons that are injected into the nanocrystals make the material n-type doped, cations diffuse into the film to compensate the negative charges as much as possible. Adapted from [38].

The electrochemical doping is conditioned: the doping only remains as long as a bias is applied over the electrodes. As soon as the applied bias disappears, the system relaxes to its intrinsic state and the doping fades away.
However, permanent electrochemical doping has been shown to be possible by fixing the ions at a certain bias.[48] This kind of doping remains even if the film is disconnected from the potentiostat that applied the bias.

1.3 QD-based devices

As discussed in the Introduction of this thesis, (O)LEDs operate via electroluminescence. For efficient operation, the injected electrons and holes need to recombine within the bulk of the active layer of the device. This prevents undesired electroluminescence quenching of the charge carriers at the electrode interfaces.[49] This can be ensured by designing a(n) (O)LED with a pre-made p-n junction (i.e. through lattice doping). If lattice doping is impractical or impossible (as is the case in OLEDs), care must be taken to balance charge carrier injection and charge carrier transport through the incorporation of multiple carrier injection and transport materials.

When considering direct electroluminescence from QDs in a LED device structure, lattice doping is impractical for aforementioned reasons (see section **1.2.1 Doping of QD films**). Therefore, QD-based LEDs so far have employed a multilayer structure, similar to those found in OLEDs.[50-54] The layers complicate the device structure of (O)LEDs tremendously and result in high cost of production.

An inherent problem that arises in all QD-based devices is the fact that QD films are not very conductive. For a thin film of QDs to be conductive (enough), the electrons need to tunnel from dot to dot. The tunneling probability of this process is quadratically dependent on the interdot distance and results in conductivities of QD films that are inferior to that of bulk semiconductors, where the charge carriers can simply move through the lattice.[55, 56] To decrease the distance, and thus to increase the conductivity, shorter ligands can be attached to the QD surface.[57, 58] Alternatively, ligands can be crosslinked to pull the QDs closer together.[59]
Even after these modifications, conductivities of QD films are still low. Therefore, only extraordinarily thin layers can be used in QD-based LEDs. To meet the demands for charge carrier injection and charge carrier transport, up to four supplementary layers may be needed. Because of the layers, (O)LEDs only emit light at forward bias. At reverse bias, charge carriers are not injected efficiently, leading to diode-like behavior.

In a LEC device structure, a (solid) electrolyte is mixed with a luminophore to facilitate charge carrier injection, theoretically eliminating the need for additional charge carrier injection and/or charge carrier transport layers. QD films, being a porous material, could be combined with an electrolyte and fitted in the LEC device structure.

In LECs, the addition of a solid electrolyte results in two advantages. When a bias is applied, the ions form an EDL at the electrode-semiconductor interface, reducing the charge carrier injection barriers. Hereafter, the device becomes electrochemically doped and cations and anions spatially become fully separated, resulting in a p-n junction. This leads to increased conductivity of the active layer for both charge carriers, and a place to safely recombine away from the interfaces.
Since a p-n doped QD film has enhanced conductivity, the active layer can be much thicker in QD-based LECs when compared to QD-based LEDs. This gives rise to a more robust device since the active layer thickness is not limiting the conductivity of the film as much as is the case for QD-based LEDs. The additional layers for charge carrier injection and transport are also redundant. Now, only three layers are needed: the active layer sandwiched between two electrodes. This device structure is simpler compared to traditional QD-based LEDs and lowers the cost of production significantly.
In contrast with LEDs, three-layered LECs are symmetrical: forward and reverse bias lose their meaning as the p-n junction is only formed after the voltage has been applied. The only asymmetry that can arise here is when two differing electrodes are chosen with dissimilar work functions.

1.3.1 Device physics of light-emitting electrochemical cells

The device physics of LECs are far from fully understood. For fifteen years, the potential profile within operational LECs has been explained by two discrepant models: the electrodynamic model (EDM)[60, 61] and the electrochemical doping model (ECDM).[62, 63] The two models are visualized in **Figure 1.3.1**.

In the EDM, a rather thick EDL is formed which causes the potential to drop drastically at the electrode/active layer interface. The bulk material is shielded from the external electric field by this EDL. This results in an electronic current in the bulk that is diffusion dominated. There is no buildup of net space charge in the bulk since the electronic carriers are compensated by cations and anions that are free to diffuse in this regime. The current

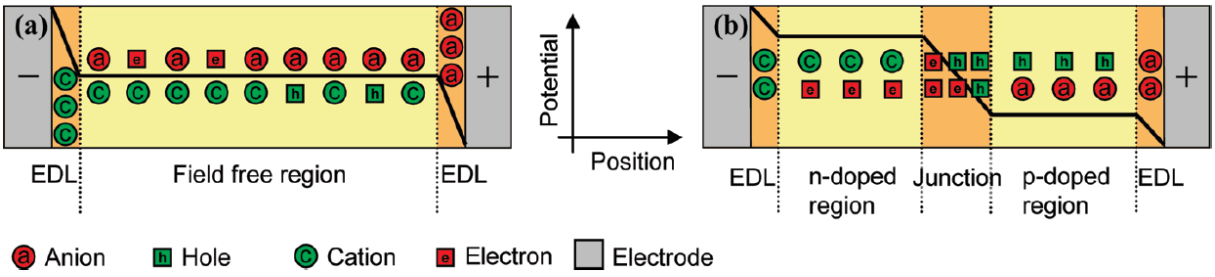

Figure 1.3.1. Steady-state potential profiles as predicted by the **(A)** EDM and **(B)** ECDM. The black line embodies the potential profile. The areas experiencing low and high electric field are marked yellow and orange, respectively. Charge neutrality is maintained in the low electric field regions. The forecasted current density and recombination rate are higher for the ECD. Reprinted from [64].

density is low as it is limited by the diffusion of the ions.

In the ECDM, the EDL that forms is less thick when compared to the EDL that forms in the EDM. The EDL is only thick enough to form an Ohmic contact between the semiconductor in the active layer and the electrode. To minimize the buildup of net space charge in the bulk when charge carriers are injected, the ions respond accordingly. Cations and anions migrate to the opposite electrode of where holes and electrons are injected, respectively. As a result, regions arise where charge carriers are electrostatically compensated by the appropriate ion. In other words, the active layer becomes electrochemically doped. The number of ions in the active layer is limited and the number of charge carriers that are injected is not (as long as the bias is applied). This eventually leads to the complete spatial separation of cations and anions.[32] Due to the relatively high concentration of charge carriers in the doped regions, the current density that can be reached is higher than the one in the EDM. In between the p-type and n-type doped regions a slim intrinsic area develops where the residual potential drops and where the holes and electrons recombine. A p-i-n junction is formed. This intrinsic region is where the light-emission takes place if the recombination is of radiative nature.

In 2010, Reenen et al. came up with a unifying model to explain the potential profile in steady-state LECs.[64] Within this model, the EDM and the ECDM turn out to be limiting situations distinguished by the charge carrier injection rate at the electrodes. If large barriers (small injection rate) for charge carrier injection exist, the EDM holds. When the barriers are low (large injection rate) and Ohmic contacts are established, the ECDM holds true.

1.3.2 LEC performance

The performance of solid-state light-emitting devices is often determined through a couple of measurements.
The first is a current-voltage (I-V) measurement. Here, the response of the current is followed as the applied bias voltage over the electrodes is increased or decreased. The rate at which the bias is changed needs to be sufficiently slow for the ions to be able to migrate to the metal contacts. Only in this way a p-i-n junction can be formed effectively.
I-V curves of LECs consist out of several domains. The domains are predicted by numerical modeling and are backed up by experimental work. [61, 65-69]
I-V curves gathered through numerical modelling as well as experiments that show the symmetry of three-layered LECs as well as the three characteristic domains of a typical LEC I-V curve are shown in **Figure 1.3.2.1**.
At the start of an I-V scan, at low applied biases, the ions are still distributed uniformly over the active layer. The barriers for charge carrier injection are thus high and the EDM applies here. The current density measured is typically low since it is diffusion limited.
Then, for applied bias voltages around the bandgap of the light-emitting species, which is usually around 2 eV for common luminophores,[49] the current density starts increasing exponentially. This is caused by the fact that the doping density increases exponentially when the applied bias nears the band gap energy. The electrochemical doping increases and the p-n junction starts to form. Barriers for charge carrier injection start to drop as the doping increases. Ohmic contacts arise and the EDCM regime is applicable.
Finally, at large applied biases, the p-i-n junction is fully formed, and steady state is reached. As no more ions can migrate towards either one of the electrodes, the increase in bias voltage does not result in an exponential

increase in current density anymore. The curve levels off.

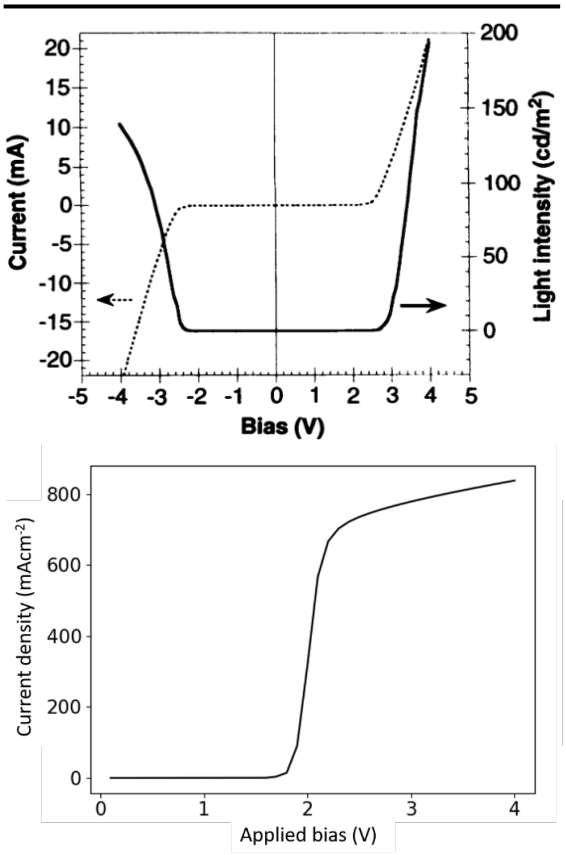

Figure 1.3.2.1. I-V curves of LECs obtained through CV and numerical modeling. (*top*) Experimental I-V curve of the first three-layered LEC using MEH-PPV as its only luminophore at an unspecified scan rate. The curve shows symmetry in current density as well as light intensity emitted. The final stage of a typical I-V curve is not visible here. Reprinted from [13]. (*bottom*) Simulated steady state I-V curve using parameters that resemble those of CdSe quantum dots and a scan rate of 0.1 V/s.

Instead of increasing the voltage linearly from zero to a given value, a procedure called a linear sweep, an I-V curve can also be recorded via cyclic voltammetry (CV). Here, the applied bias is increased linearly from zero to a given positive value, but hereafter the applied bias is lowered linearly back to zero. The same procedure is then repeated to negative potentials. In this way it can easily be checked if diode-like behavior arises and how reversible the electrochemical doping of the device is. In addition, the current density can be found with I-V curves.

Whilst I-V curves provide information on what is happening within the device, other measurements can deliver information on the optical performance of the LECs.

While performing an I-V curve, the intensity of the light emitted can be measured. In this way, the turn-on voltage and the relation between current density and light emission intensity can be determined.

The electroluminescence spectrum can also be recorded when applying a certain bias voltage and compared to the photoluminescence spectrum of the luminophore.

Finally, the optical measurements mentioned above can be performed at constant applied voltage. In this way the turn-on time, behavior over time and lifetime of the device can be determined.

2 Experimental

All materials used during this thesis are listed in section **2.1 Materials**. Section **2.2 Quantum dot synthesis** describes the synthesis of CdSe/CdS/ZnS QDs as well as their ligand exchange and the synthesis of ZnO QDs. The fabrication of LECs is discussed in section **2.3 LEC fabrication**. Finally, the instruments and setups used to gather all results are discussed in section **2.4 Measuring methods**.
All procedures were carried out in a nitrogen filled glovebox ([O_2] < 1 ppm and [H_2O] < 1 ppm) unless stated otherwise.

2.1 Materials

The following materials were used without further purification: 1-butanol (BuOH, 99.8%, Sigma-Aldrich), 2-propanol (IPA, technical grade, VWR international B.V.), acetone (technical grade, VWR international B.V.), aluminum (Al pellets, 99.99% pure, Kurt J. Lesker), anhydrous acetonitrile (ACN, 99.8%, Sigma-Aldrich), anhydrous methanol (MeOH, <0.003% H_2O, Sigma-Aldrich), anhydrous methyl acetate (>99%, Acros organics), anhydrous N,N-Dimethylformamide (DMF, 99.8%, Sigma-Aldrich), anhydrous toluene (≥99.5%, VWR international B.V.), cadmium oxide (CdO, 99.998%, Puratronic), deuterated acetonitrile (ACN-d3, 99.8% D, TCI Europe N.V.), deuterated toluene (tol-d8, 99.5% D, Eurisotop), ethanol (EtOH, Sigma-Aldrich), hydrochloric acid (HCl, ~37%, Fisher Scientific), nitric acid (~65%, Acros Organics), octadecylamine (ODA, 97%, Sigma-Aldrich), poly(3,4-ethylenedioxythiophene):polystyrenesulfonate Al 4083 (PEDOT:PSS, Osilla), potassium hydroxide (KOH pellets, 99.99%, Sigma-Aldrich), propionic acid (PA, ≥99.5%, Sigma-Aldrich), selenium (Se, 99.99%, Sigma-Aldrich), sulfur (S, ≥99.99%, Sigma-Aldrich), tri-n-octylphosphine (TOP, >85%, TCI Europe N.V.), triethyloxonium tetrafluoroborate (triBF$_4$, ≥97%, Sigma-Aldrich), trioctylphosphine oxide (TOPO, 99%, Sigma-Aldrich), zinc acetate (99.99%, Sigma-Aldrich), zinc acetate dihydrate (reagent grade, Sigma-Aldrich).
The solids lithium trifluoromethanesulfonate ($LiCF_3SO_3$, 99.99%, Sigma-Aldrich) and poly(ethylene oxide) (PEO, average M_v ~ 5.000.000, Sigma-Aldrich) were kept under vacuum overnight before being introduced into the glovebox.
The liquids 1-octadecene (ODE, synthesis grade, Sigma-Aldrich), oleic acid (OA, 90%, Sigma-Aldrich) and oleylamine (OLAM, 70%, Sigma-Aldrich) were heated *in vacuo* until bubble formation was not observed anymore before being introduced into the glovebox.

2.2 Quantum dot synthesis

All syntheses described hereafter were carried out on a Schlenk line under inert atmosphere.

2.2.1 CdSe/CdS/ZnS QDs

The luminophore used in the LECs produced in this thesis are CdSe/CdS/ZnS core/shell/shell QDs. Their synthesis is adapted from a hot injection method designed by Qu et al.[70] The synthesis comprises of three steps: CdSe core synthesis, shelling the cores with CdS and shelling the CdSe/CdS core/shell QDs with a second shell of ZnS.

2.2.1.1 CdSe core synthesis

To yield the Se precursor (1.19M SeTOP in ODE), 1.42 g Se, 7.50 g TOP and 11.90 g ODE were combined in a 40 mL vial. The mixture was stirred at 90 ℃ until all Se was dissolved, resulting in a colorless solution. The precursor was stirred at 100 ℃ before usage in the synthesis.
To obtain the cadmium precursor (0.1M cadmium oleate in ODE), 0.51 g (5.00 mmol) CdO, 4.48 g OA and 15.78 g ODE were combined in a 100 mL three-neck round-bottom flask. The mixture was then heated to 200 ℃ under N_2 atmosphere for 30 minutes. Hereafter, the mixture was cooled to 120 ℃ and degassed *in vacuo* for 30 minutes. These two steps were repeated once more, until the brownish color of the CdO had disappeared and a colorless solution was left. The mixture was cooled to room temperature, put under vacuum, and transferred into a glovebox. The precursor was stirred at 100 ℃ before usage in the synthesis.
Then, 3.20 g ODA and 1.11 g TOPO were combined in a 100 mL three-neck round-bottom flask outside the glovebox. The flask was transferred to a Schlenk line and degassed *in vacuo* at 150 ℃ for 45 minutes. The temperature was then lowered to 100 ℃ for three hours. An hour before the hot injection started, the temperature was again raised to 140 ℃. After this hour, the flask was filled with N_2 and 5.20 g of the Se precursor was added through a 20 mL syringe. Stirring was set at 650 RPM. Next, the temperature was raised to 300 ℃. As soon as the temperature hit 300 ℃, 4.90 g of the cadmium

precursor was quickly injected in the middle of the reaction mixture through two 20 mL syringes. The solution turned dark immediately, and the temperature dropped to ±260 ℃. The temperature was raised to 280 ℃ and the QDs were grown for four minutes.
After the reaction was completed, the temperature was quickly lowered to room temperature with an air gun. When the temperature had dropped to 50 ℃, 5 mL anhydrous toluene was added to fully quench the reaction. The reaction slurry is shown in **Figure 2.2.1.1.1**.

Figure 2.2.1.1.1. (*left*) CdSe core reaction slurry right after quenching the growth reaction. (*center*) CdSe core solution in anhydrous toluene after purification. (*right*) CdSe core solution in anhydrous toluene after purification and illuminated with a 405 nm blue laser. The solution after purification has a concentration of 73.2 µM.

It was divided over two 40 mL vials that were flushed with N_2 three times and transferred into a glovebox. 20 mL of anhydrous methyl acetate and 4 mL of MeOH were added to each vial to purify QD mixture. The vials were centrifuged outside the glovebox for six minutes at 3800 RPM in an Eppendorf Centrifuge 5804. The vials were transferred back into the glovebox, where the supernatant was discarded. The dots were redispersed in 8 mL anhydrous toluene and this procedure was repeated once. The final QD solution is shown in **Figure 2.2.1.1.1**.

2.2.1.2 CdS shelling

To obtain the sulfur precursor (0.5M S in ODE), 0.32 g S and 15.78 g ODE were combined in a 40 mL vial. The precursor was stirred at 130 ℃ until all sulfur was dissolved before the precursor was used in the synthesis.
Then, 1.64 mL of CdSe core solution (73.2 µM), 2.34 g ODE and 3.75 mL 0.1M cadmium oleate in ODE were added to a three-neck round-bottom flask. The addition of extra ligands in the form of cadmium oleate was found to be crucial for the QDs to remain stable at elevated temperatures. The flask was connected to a Schlenk line and flushed with N_2 three times. Hereafter, the mixture was degassed *in vacuo* at 60 ℃ for 30 minutes whilst stirring at 340 RPM. The temperature was raised to 310 ℃, and as soon as the temperature reached 230 ℃, precursor addition was initiated. At a rate of 2 mL/hour, 6 mL of a combination of 3.12 mL cadmium precursor and 3.06 g ODE (resulting in a 0.04M solution) and 6 mL of a combination of 0.62 mL S precursor and 5.03 g ODE (resulting in a 0.04M solution) were added to the reaction mixture using syringe pumps. A photograph of this setup is shown in **Figure 2.2.1.2.1.**

Figure 2.2.1.2.1. Shelling of QDs using syringe pumps.

During the shelling, the photoluminescence (PL) of the QD mixture was checked by shining a blue laser on the mixture. The PL increased during the shelling. After 2.25 hours, the stirring speed was increased to 450 RPM. After 3 hours, the reaction mixture was cooled down to room temperature with an air gun and divided over two 40 mL vials that were flushed with N_2 three times. 15 mL anhydrous methyl acetate and 3 mL MeOH were added to the vials, and they were centrifuged for six minutes at 3800 RPM. A two-layered system formed, with the QDs at the interface and in the top layer. The lower phase was discarded as carefully as possible, and 4 mL toluene was added to the remaining solution. This purification step was repeated one more time before moving on to the second shelling.

2.2.1.3 ZnS shelling

To make the zinc precursor (0.5M zinc oleate in ODE), 1.84 g zinc acetate, 15.78 g ODE and 5.65 g OA were added into a 100 mL three-neck round-bottom flask. The flask was

connected to a Schlenk line, and the mixture was degassed *in vacuo* at 130 ℃ for two hours. The mixture was cooled down and transferred into a glovebox, where the contents were poured into a 40 mL vial. A fraction of the 0.5M precursor was diluted with ODE to yield a 0.1M zinc precursor. The precursor was stirred at 130 ℃ before usage in the synthesis.
Then, 3.75 mL of 0.1M zinc oleate, 2.37 g ODE and the contents of the solution after the CdS shelling were added to a 100 mL three-neck round-bottom flask. The flask was transferred to a Schlenk line, flushed with N_2 three times, and degassed *in vacuo* at 60 ℃ for 30 minutes. The flask was filled with N_2, and the temperature was raised to 290 ℃ while stirring at 490 RPM. As soon as the temperature reached 230 ℃, precursor addition was started. At a rate of 0.67 mL/hour, 1 mL of a combination of 1.94 mL 0.1M zinc precursor, 0.43 g OLAM and 0.05 g ODE (resulting in a 0.38M solution) and 1 mL of a combination of 0.97 mL 0.5M S precursor and 0.81 g ODE (resulting in a 0.24M solution) were added to the reaction mixture using syringe pumps.
After 90 minutes, the reaction slurry was cooled down to room temperature with an air gun and divided over two 40 mL vials that were flushed with N_2 three times. A photograph of the QDs right after cooling the reaction slurry down to room temperature is shown in **Figure 2.2.1.3.1**.

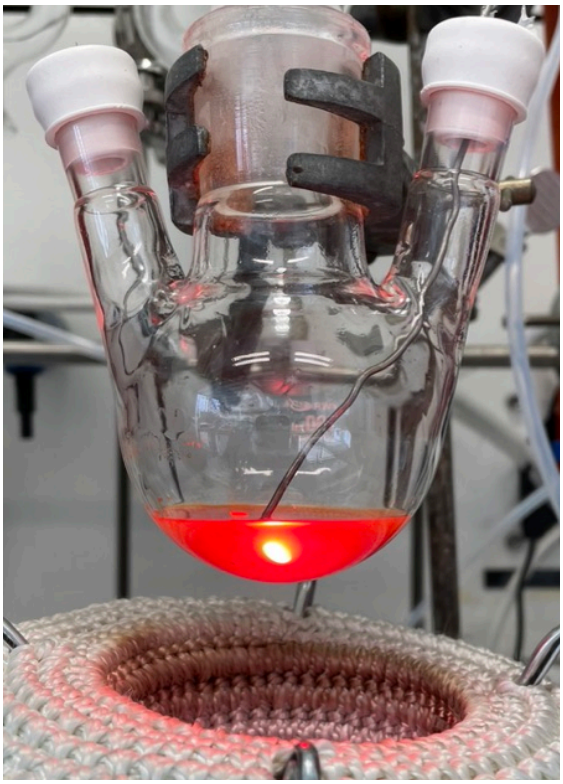

Figure 2.2.1.3.1 CdSe/CdS/ZnS reaction slurry right after cooling down to room temperature. The solution is illuminated with a 405 nm blue laser.

The solutions were purified in the same way as the mixture after the CdS shelling. The same two-layered system appeared. After the second purification, the contents of the vials were combined, and this mixture was purified another four times with 15 mL anhydrous methyl acetate and 3 mL MeOH. The QDs were redispersed in 4 mL hexane. This solution had a concentration of approximately 40.08 mg/mL.

2.2.2 Ligand exchange

A ligand exchange was adapted from a method by Dong et al.[71]

Typically, 1 mL of the CdSe/CdS/ZnS dispersion in hexane was added to a 40 mL vial and diluted with 7 mL hexane. To this dispersion, 7 mL of 0.01M $triBF_4$ in DMF was added, resulting in a two-layered system with the QDs dispersed in the top layer. 1.5 mL of 0.07M propionic acid in DMF was also added to this mixture and the solution was stirred vigorously at 90 ℃.
After 45 minutes, the solution was taken from the hot plate. Upon cooling, the two-layered system formed again with the QDs in the lower layer. If the QDs did not transfer to the polar phase, extra $triBF_4$, extra acid and extra hexane can be added.
To purify the reaction mixture, the contents of the vial were divided over two 50 mL centrifuge tubes. Anhydrous toluene was added to fill the tubes completely and they were centrifuged at 5000 RPM for six minutes. The supernatant was discarded, and the LE was repeated once more.
Hereafter, the QDs were extremely soluble in acetonitrile and redispersed in 2 mL of this solvent, resulting in a colloidal dispersion with a concentration of roughly 8.1 mg/mL.

2.2.3 ZnO QDs

The synthesis of ZnO QDs was carried out *via* an adaptation to a procedure described by Lim et al.[72] Typically, 1.00 g zinc acetate dihydrate and 40 mL EtOH were combined in a 100 mL three-neck round-bottom flask. The mixture was stirred and heated at 60 ℃ within a fume hood. In a separate Erlenmeyer, 0.52 g KOH was dissolved in 20.7 mL MeOH. This mixture was also stirred and heated at 60 ℃ within a fume hood. When both reagents had fully dissolved, the contents of the Erlenmeyer were added to the round-bottom flask dropwise. Hereafter, the solution was stirred at 60 ℃ for another 90 minutes. The resulting solution was

cooled to room temperature and looked milk-like. The solution was centrifuged at 3800 RPM for six minutes and consequently purified with MeOH once. The purified ZnO QDs were redissolved in 2 mL 1-butanol.

2.3 LEC fabrication

The LECs fabricated hereafter all make use of an indium tin oxide (ITO) covered glass substrate with a length of 2.54 cm and a width of 1.18 cm.

2.3.1 Half-etching

To prevent direct short circuits between the contact of the potentiostat and the ITO, part of the ITO can be etched away with aqua regia.
Typically, 3 mL nitric acid and 9 mL hydrochloric acid were combined in a beaker and shaken gently. Part of the contents of this beaker were poured into a petri dish, until the liquid reached a height of about 0.8 cm. Then, the ITO substrate was placed in the liquid horizontally and left there for about five minutes. Next, the ITO substrate was rinsed with demineralized water and dried. A multimeter was used to check whether the ITO was etched away sufficiently. If not, the ITO substrate was placed in the aqua regia solution for a few minutes longer. After the etching, the ITO substrate was thoroughly rinsed with demineralized water and dried. A photograph of a half-etched ITO substrate is shown in **Figure 2.3.1.1**.

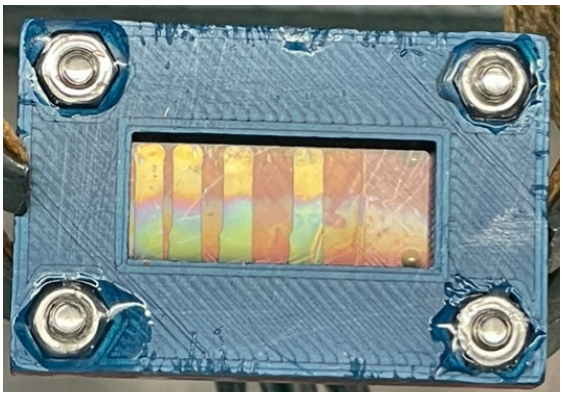

Figure 2.3.1.1. Photograph of a half-etched LEC placed in the cap used for doing measurements on the LECs. The ITO has a blueish color and runs until approximately half the Al stripes. Details on the cap and its design are provided later in this thesis.

After the etching, the ITO substrate was subsequently sonicated for ten minutes in water, IPA, acetone, and IPA. After the final sonicating step, the ITO substrate was placed in an ozone cleaner for 20 minutes to ensure wettability with polar solvents.

2.3.2 Hole injection layer

Typically, the ITO substrate is placed on a spin coater inside a fume hood and 100 µL of PEDOT:PSS solution is deposited on the ITO substrate. After spinning for 40 seconds at 4000 RPM, the ITO substrate is transferred to a glovebox and dried at 200 ℃ for 15 minutes. These conditions were found to be optimal for surface roughness and conductivity.[73, 74] A uniform, transparent film forms with some buildup and thus blue color on the corners of the ITO substrate.

2.3.3 Active layer

To yield the master solution used for spin coating, the CdSe/CdS/ZnS solution after LE (8.1 mg/mL), a solution of $LiCF_3SO_3$ (10 mg/mL in ACN) and a solution of PEO (10 mg/mL in ACN) were combined in a 20:1:5 volume ratio. The PEO solution had to be stirred at 90 ℃ for several hours to become fully dissolved before being used in the master solution. The master solution was shaken vigorously to ensure good homogenization of the chemicals.
Typically, the ITO substrate is placed on a spin coater and 100 µL of master solution is deposited on the ITO. Using less master solution might result in non-homogeneous films after spin coating. After spinning the ITO at 2000 RPM for two minutes and 4000 RPM for one minute, it was dried at 90 ℃ for 30 minutes. This combination of rotation speeds and times was found to result in the best-looking films. Another layer was deposited and dried on the previous layer in the same manner as described above to prevent pinholes from forming. A uniform, transparent film is formed with a red glow that shows uniform PL upon illumination with a blue laser.

2.3.4 Electron injection layer

Typically, the ITO substrate is placed on a spin coater and 100 µL of ZnO QD solution is deposited on top of the active layer. After spinning the ITO substrate at 4000 RPM for one minute, it was dried at 120 ℃ for 30 minutes, resulting in a uniform, transparent film.

2.3.5 Cathode

To deposit the Al cathode, 5,000 - 10,000 Å Al was deposited on the ITO substrate under high vacuum (~10^{-6} mbar) whilst rotating the holder at 15 RPM. This resulted in mirror-like Al stripes as can be seen in **Figure 2.3.1.1**.
A schematic of the final sandwich structure achieved after all layers are deposited on top of the ITO substrate is shown in **Figure 2.3.5.1**.

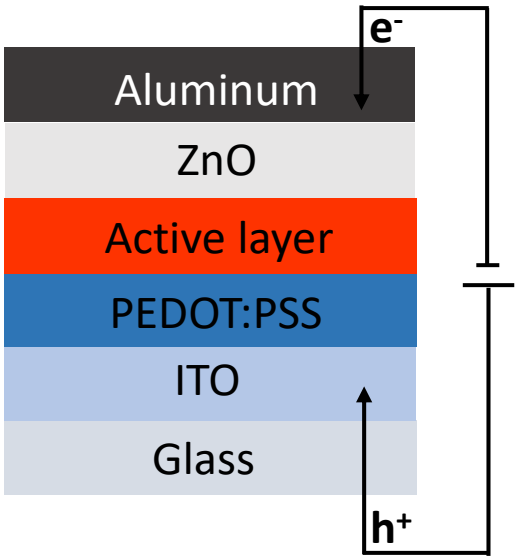

Figure 2.3.5.1. Schematic of the final sandwich structure achieved by the sequential deposition of all the layers. The schematic shows a non-etched LEC with two charge carrier injection layers. It is also shown how contact with the potentiostat is established and where the charge carriers are injected.

2.4 Measuring methods

The adsorption spectrum versus a reference of the pure solvent was measured in a PerkinElmer UV/VIS Lambda 365 for wavelengths between 300 and 700 or 800 nm.

Fluorescence measurements were recorded on Edinburgh Instruments FLS980 spectrometer equipped with a PMT 400 detector. PLQYs were measured against a rhodamine 6G dye solution in ethanol at an excitation wavelength of 499 nm. The PLQY of rhodamine 6G is around 95%.
Solution NMR spectra were recorded on an Agilent 400-MR DD2 equipped with a 5 mm ONE NMR Probe and operating at 25 °C. ^{1}H NMR (399.7 MHz) spectra were collected with a recycle delay of 1 s in deuterated toluene (before LE) or deuterated acetonitrile (after LE). Signals were referenced according to the residual methyl peak of toluene (2.08 ppm). ^{19}F NMR spectra (367.04 MHz) were collected on the same machine with a recycle delay of 1 s.

I-V curves were recorded through voltametric linear sweeps as well as voltametric cycles by connecting the LECs to a PGSTAT128N Autolab potentiostat and scanning with a scan rate of 0.03 V/s. The measured current was converted to a current density in mAcm^{-2} by dividing by the area that was emitting photons during the measurement. For non-etched LECs the area of a whole stripe was calculated. For half-etched LECs this area was estimated using photos of the LECs under operation.
A special cap was designed for this purpose. A schematic of the cap is shown in **Figure 2.4.1**.

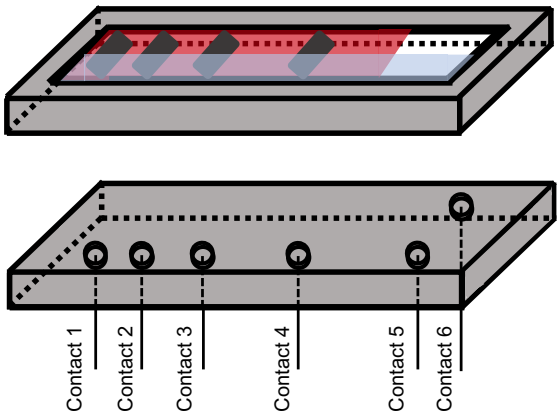

Figure 2.4.1. Schematic of the cap used for measurements on the LECs. The four holes drilled on the four edges to be able to screw the two parts of the cap together are not shown for clarity. (*top*) The top part of the cap with a half-etched LEC placed in it. The aluminum stripes that contact pogo pin contacts 1 - 4 are shown as dark grey stripes. The active layer is colored in red. The ITO is shown in light blue. The cap needs to be rotated 180° towards the reader to be placed correctly. (*bottom*) Part of the cap that is connected to the potentiostat via pogo pins.

Before device construction, about half of the ITO that is deposited on the glass substrate can be etched away with aqua regia. As can be seen in **Figure 2.4.1**, pogo pin contacts 1 – 4 are placed lower than the middle of the cap. Because of this, the pogo pins cannot contact the ITO if they were to pierce through the aluminum (and other layers). The half-etching in combination with the cap design prevents direct short circuits between the pogo pin and the ITO.
The half-etching was not found to be necessary for successful LEC fabrication. However, it enhances the chance of fruitful operation since direct short circuits are excluded from arising.

When the LEC is placed in the cap, contact 6 and one of the contacts 1 – 4 are connected to the potentiostat. If the Al stripes are deposited at the right position, each of the four contacts can be used. Contact 6 is set as working electrode, while one of the other contacts is fixed as reference and counter electrode. In this way, scanning to positive applied biases results in hole injection at the ITO contact and electron injection at the Al contact.

The EL spectrum was recorded by placing the LEC in the cap within a glovebox, applying parafilm around the edges of the cap and taking the cap outside the glovebox. Then, the cap was clamped, and a Si fiber photodiode was placed directly on top of the glass at the stripe that would irradiate light. The fiber was connected to a USB2000+ fiber optic spectrometer from Ocean Optics. Finally, a constant voltage was applied for 70 seconds, and the EL spectrum was recorded for 60 seconds. The whole setup was wrapped in a black cloth to ensure background lighting was minimalized as much as possible.

3 Results and discussion

The results gathered during this thesis are shown and discussed in this chapter. The results of the CdSe/CdS/ZnS QD synthesis and the ligand exchange carried out on them are shown and discussed in sections **3.1 CdSe/CdS/ZnS synthesis** and **3.2 Ligand exchange**, respectively. In the final section, **3.3 LECs**, the results of the operation of the LECs fabricated are shown and discussed.

3.1 CdSe/CdS/ZnS synthesis

3.1.1 CdSe cores

As a measure of quality of the synthesized CdSe QDs, absorption spectra were recorded, which are shown in **Figure 3.1.1.1** for CdSe core QDs and in **Figure 3.1.2.1** for the CdSe/CdS/ZnS core/shell/shell QDs. In the first figure, a clear first absorption maximum can be observed at 572 nm with a HWHM of 13 nm. This confirms that a monodisperse set of core QDs was obtained.

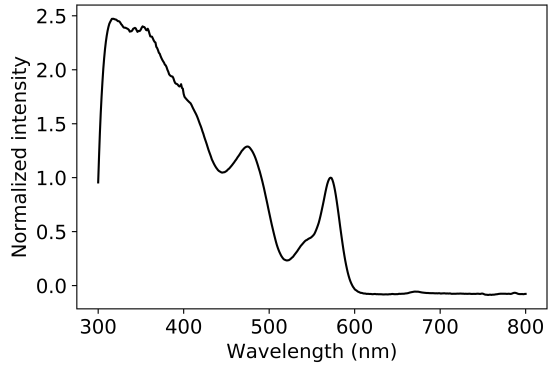

Figure 3.1.1.1. Adsorption spectrum of the final CdSe core solution. The intensities are normalized compared to the first absorption maximum.

3.1.2 CdSe/CdS/ZnS QDs

The adsorption spectrum of the final CdSe/CdS/ZnS solution before performing the LE is shown in **Figure 3.1.2.1.**

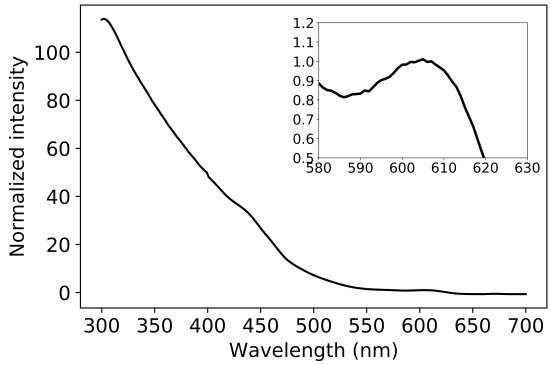

Figure 3.1.2.1. Adsorption spectrum of the final CdSe/CdS/ZnS solution. The intensities are normalized compared to the first absorption maximum. The inset shows an amplification of the 580 – 630 nm range.

The 1S adsorption peak is shifted to 607 nm after the shellings. The HWHM of the core adsorption peak remained 13 nm after the shellings. **Figure 3.1.2.1** shows strong adsorption at low wavelengths next to the adsorption maximum of the core. This adsorption arises because of the shells, which have a larger bandgap and therefore adsorb at lower wavelengths. The adsorption spectrum therefore indicates that shell incorporations were successful. The adsorption of the shells coincides with the adsorption of the peak, resulting in less distinct core adsorption maxima compared to **Figure 3.1.1.1**. The PLQY of the core/shell/shell QDs was measured to be 86% vs. rhodamine 6G.

3.2 Ligand exchange

Devices that were constructed with as-synthesized QDs could not be operated fruitfully. Therefore, a LE was designed, based on the one reported by Dong et al.[71]

The ^{1}H-NMR spectrum of the CdSe/CdS/ZnS QDs before and after LE as well as the ^{19}F-NMR spectrum after LE are shown in **Figure 3.2.1**. The ^{19}F-NMR spectrum before LE did not show any significant signal and this spectrum is therefore not reported.

In the ^{1}H-NMR spectrum before the LE, the

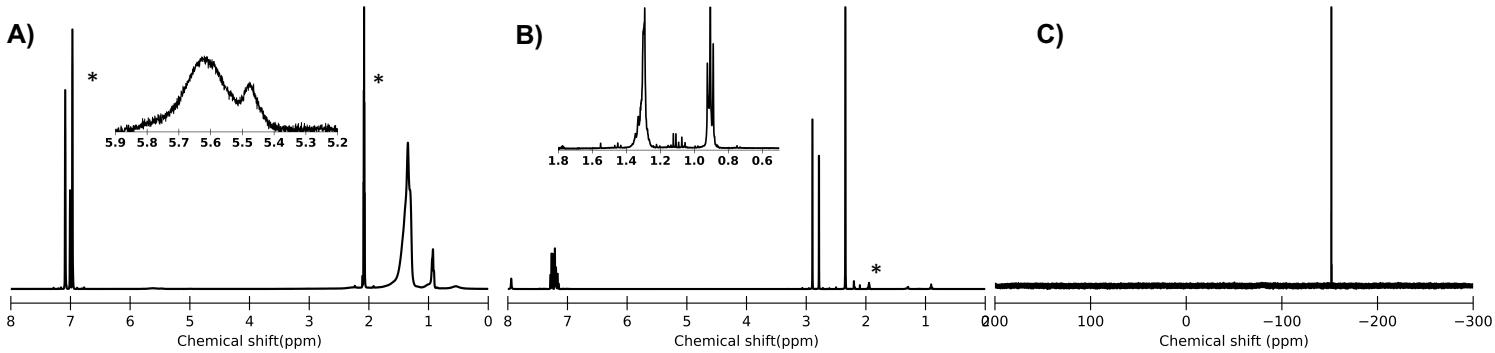

Figure 3.2.1. (A) ^{1}H-NMR spectrum of the CdSe/CdS/ZnS QDs before LE. The inset shows an amplification of the 5.2 – 5.9 ppm range. The solvent peaks are indicated with an asterics. **(B)** ^{1}H-NMR spectrum of the CdSe/CdS/ZnS QDs after LE. The inset shows an amplification of the 0.5 – 1.8 ppm range. The solvent peak is indicated with an asterics. **(C)** ^{19}F-NMR spectrum of the CdSe/CdS/ZnS QDs after LE.

peaks around 2.1 ppm and 7 ppm are attributed to the solvent.[75] The long, apolar hydrocarbon ligands show up as broad peaks at around 0.9 ppm and 1.3 ppm. Another weak signal arises at ~5.6 ppm, typical for the double bond present in oleate ligands present on these nanocrystals.[76] The peaks are broad, indicating that the ligands are strongly bound to the surface of the QDs.
For the ^{1}H-NMR after the LE, the peak around 1.94 ppm is attributed to the solvent.[75] The peaks around 2.8 ppm, 2.9 ppm and 7.9 ppm are accredited to residual DMF. The peaks around 2.3 ppm and 7.2 ppm are ascribed to residual toluene. The peak around 2.1 ppm is attributed to water. The long, apolar hydrocarbon ligands that showed broad peaks around 0.9 and 1.3 ppm are almost completely gone. The signal at approximately ~5.6 ppm that is typical for the double bond present in oleate ligands has completely vanished. The triethyloxonium cation is not observable in the spectrum since this cation should result in a quartet at ~4.68 ppm and a triplet at ~1.53 ppm.[77] Apparently, the cation has been completely washed away in the purification step.

The ^{19}F-NMR after LE shows a sharp peak at -151.8 ppm. This peak is attributed to BF_4^- anions.[78] The peak is sharp, indicating that the anions bind to the QD surface in a weak fashion. This conclusion agrees with the findings of Dong et al. on their LE.

The peaks that are characteristic for the hydrocarbon ligands almost completely disappeared in the ^{1}H-NMR spectrum and a sharp BF_4^- peak in the ^{19}F-NMR spectrum appeared after the LE. This indicates that the LE strips the native ligands from the QD surface almost completely and replaces them by BF_4^- anions that bind to the surface of the QDs weakly.

In 2010, Dong et al. demonstrated that the long, apolar hydrocarbon ligands that passivate the surface of several differing types of nanocrystals can be removed and replaced by BF_4^- anions.[71] They performed a ligand exchange with $NOBF_4$ and showed that the interparticle spacing had reduced from 3.0 nm to 1.2 nm. The nanocrystals were soluble in multiple polar solvents after the LE. They confirmed the removal of the native ligands and the replacement by BF_4^- anions with FTIR spectroscopy.

The FTIR measurements showed no bands that could be ascribed to the NO^+ cation after the LE. Dong and coworkers hypothesize that the NO^+ cations, together with the BF_4^- anions, react with solvated water molecules towards nitrous acid and fluoroboric acid, creating a rather acidic environment. This acidic environment is confirmed by the researchers, as pH values of ~3 – 5 were measured, even after purification. The protons in solution are hypothesized to protonate the native ligands and therefore remove them from the surface. Consequently, the BF_4^- anions can coordinate to the nanocrystal surface as they are abundantly present in the solution.
Although no NO^+ cations could be found with FTIR measurements, **ζ**-potential and electrophoretic measurements showed that the surface of the nanocrystals was positively charged when dispersed in DMF. Dong et al. attribute this positive charge to undercoordinated cations that arise by incomplete coverage of the nanocrystal surface by the BF_4^- anions.

The reduced spacing between nanocrystals after the LE can mean that films of these materials show higher conductivity. This is commonly desired in optoelectronic devices that incorporate these materials as their emissive species, like LEDs and LECs.

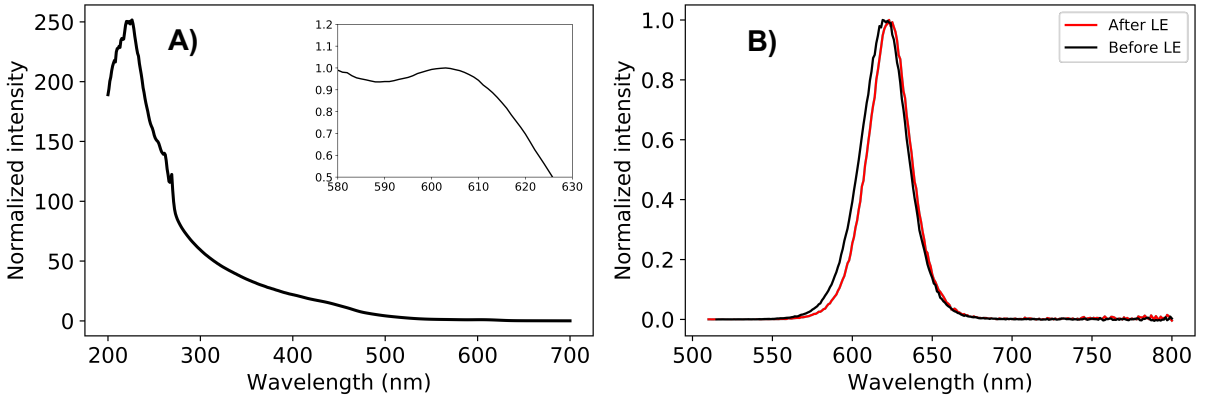

Figure 3.2.2. (A) Adsorption spectrum of the final CdSe/CdS/ZnS solution after LE. The inset shows an amplification of the 580 – 630 nm range. **(B)** PL spectra of the CdSe/CdS/ZnS QDs before and after LE. The intensities are normalized compared to the first maximum.

Therefore, I have designed a facile and robust LE that is based on the one discovered by Dong et al. The LE is essential to successful LEC fabrication with QDs as their only luminophore.

The addition of acid as well as using elevated temperatures were found to be crucial for the LE to be effective, in contrast to what was found by Dong et al. A reason for the addition of acid could be the fact that acidic conditions are needed for the native ligands to be removed effectively. Where these acidic conditions are provided by the consumption of the NO^+ cations in the case of the LE as designed by Dong and coworkers, it could very well be that these acidic conditions are not provided by the cation of $triBF_4$. Therefore, supplementary acid is needed for the LE to be effective. The need for elevated temperatures could find its root-cause in the fact that the LE on the CdSe/CdS/ZnS QDs might be more endothermic than the LE on the nanocrystals that were investigated by Dong et al. They did not perform their LE on specifically these QDs, and their activation energy might lie higher compared to the nanocrystals examined by Dong and coworkers.

The adsorption spectrum of the final CdSe/CdS/ZnS solution after LE is shown in **Figure 3.2.2A**.
The spectrum shows a core adsorption peak at 603 nm, which is a blueshift of 4 nm compared to the QDs before the LE. Next to this, a HWHM of 23 nm is observed.

A comparison of the PL of the QDs before and after the LE is shown in **Figure 3.2.2B**. The spectra show a maximum before LE and after LE at 619 nm and 623 nm, respectively. This is a redshift of 4 nm. The HWHM of the PL spectrum decreased from 18 nm to 16 nm by the LE. It is remarkable that the PL shows a redshift and a narrowing of the HWHM after the LE, while the adsorption spectrum shows a blueshift and a broadening of the HWHM.

The PLQY of the QDs after LE was measured to be 22% vs. rhodamine 6G. This is a significant drop compared to the 86% PLQY before the LE, which could be explained by the fact that the coverage of the nanocrystal surface by BF_4^- anions is incomplete, as Dong and coworkers hypothesized. This results in bare cations at the nanocrystal surface that could cause the observed positive charge of the nanoparticles. As the cations are undercoordinated, dangling orbitals arise that can introduce trap states which can significantly lower the PLQY, as described in section **1.2 Quantum dots**.

Dong et al. took TEM images of their nanocrystals before and after LE and concluded that the crystals shape and size remained unaffected after the LE. TEM images of the QDs after the LE described in this thesis were not gathered, but the results from the adsorption spectrum, the PL spectrum, and the drop in PLQY indicate that the QDs are affected by the LE. Although the exact manner in which the QDs are affected by the LE remains uncertain based on these results, some possible hypotheses are presented:

First, the acid that is added during the LE could etch away part of the ZnS shell, resulting in smaller particles with increased polydispersity. The etching of QDs by acid is namely also observed in the HF treatment of InP QDs.[79-82] The last reference also mentions broadening of the size distribution of the QDs after the etching with HF.

Second, the replacement of the ligands themselves could be responsible for the small shifts in optical properties.

3.3 LECs

The results on the operation of the three types of LECs, either with zero, one or two charge carrier injection layer(s), will now be shown and discussed.

3.3.1 Two charge carrier injection layers

To find out if the presence of electron/hole transport layers was necessary to achieve electroluminescence in QD LECs, devices both with and without an ETL and HTL were fabricated. First, devices with both an ETL and a HTL will be discussed. These consist of five layers in total: the ITO contact (on top of the glass substrate), whereafter PEDOT:PSS, master solution, ZnO QDs and Al were consecutively deposited on this layer as described in section **2.3 LEC fabrication**.
To evaluate the electrical response of this device, a CV measurement was conducted, shown in **Figure 3.3.1.1**.

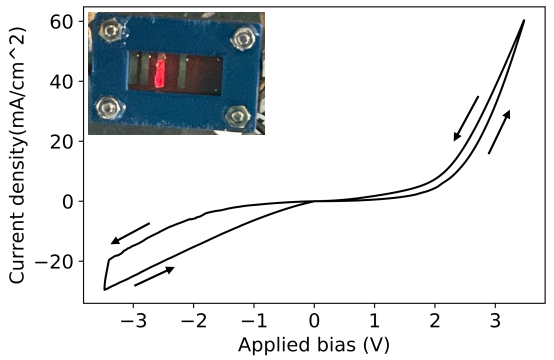

Figure 3.3.1.1. I-V curve of a LEC with two charge carrier injection layers. The curve was recorded through CV. The arrows indicate the forward and the backward part of the scan. The inset shows a photograph of the device under operation at forward bias.

The I-V curve shows diode-like behavior. Under positive bias the current densities measured are almost three times as high as under negative bias. Also, the device emits light under positive bias while it does not under negative bias. The charge carrier injection layers apparently only allow efficient charge carrier injection in one direction.
The current density found for this LEC at 3.5V is high (and perhaps even the highest) compared to other QD-based LECs with a PEDOT:PSS layer and ZnO layer as charge carrier injection layers.[21, 83] These LECs namely showed lower or comparable current densities at 3.5V.
The scan at positive bias shows reversible charging of the LEC, since the current densities on the forward part of the scan are almost equal to the current densities when going back to 0V. I hypothesize that the p-n junction needs to be formed on the forward scan, while this p-n junction is already formed during the backward scan. The presence of the p-n junction results in a more conductive film during the backward scan and therefore leads to higher current densities. This phenomenon is also observed at negative bias. However, it remains unclear why the difference in current densities at negative bias between the forward and backward scan is larger than for the scans under positive bias.
The first two domains of a typical I-V curve are clearly visible in the curve. However, the last phase in a typical LEC I-V curve, the leveling off of the curve, is not seen under both biases. This domain can however be observed at higher applied bias, as this was seen in a different experiment. Apparently, full separation of ions is not yet achieved at ±3.5V.
Although the I-V curve shown in **Figure 3.3.1.1** only uses a scan window of ±3.5V, another experiment revealed that this type of LEC can withstand applied biases of at least ±8V. The I-V curve that shows the asymptotic behavior of the current density and the enlarged stability window is shown in **Figure 3.3.1.2**.

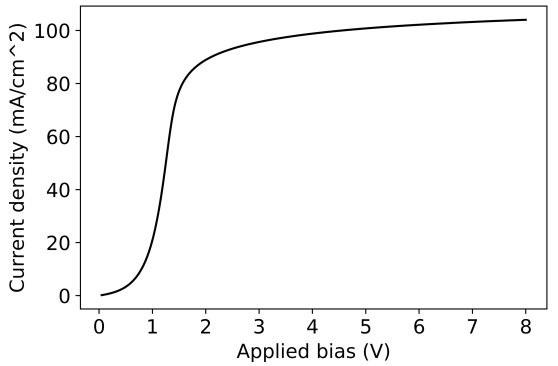

Figure 3.3.1.2 I-V curve of a LEC with two charge carrier injection layers. The curve was recorded through a linear sweep.

The shape of this I-V curve shows great resemblance with the I-V curve obtained through numerical modeling as shown in **Figure 1.3.2.1**.
The EL spectrum of this LEC was also measured. A comparison between the EL spectrum of this LEC and the PL spectrum of the QDs in solution is shown in **Figure 3.3.1.3**.

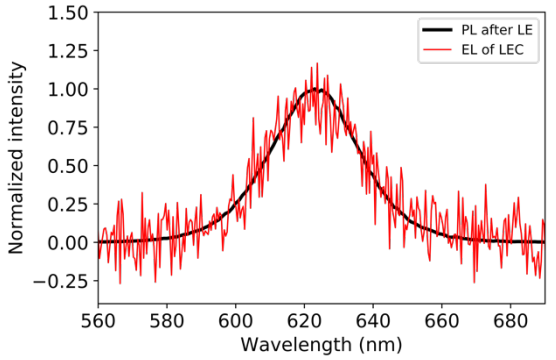

Figure 3.3.1.3. A comparison of the PL spectrum of the CdSe/CdS/ZnS QDs after LE and the EL spectrum of the LEC with two charge carrier injection layers at a constant voltage of 4V. The intensities are normalized compared to the first maximum. The EL shows a lot of noise since the absolute number of counts measured was low.

The EL spectrum and PL spectrum both show a maximum at 623 nm. The curves show great resemblance and the HWHM of both is determined to be 16 nm. From these results, the conclusion can be drawn that the EL spectrum of the LEC and the PL spectrum of its luminophore are thus indistinguishable.
The EL spectrum of **Figure 3.3.1.3** was recorded at a constant voltage of 4V. The current density leveled off to a stable 57 $mAcm^{-2}$ during this measurement. The EL spectrum was also determined for a constant applied bias of 3V and 3.5V. At 3V, the spectrum did not show a significant peak and the current density approached 22 $mAcm^{-2}$. At 3.5V, the peak started to be visible, and the current density neared 42 $mAcm^{-2}$. The turn-on voltage must thus lie somewhere between 3 – 3.5V. These results show that increasing the applied bias voltage leads to increased current densities and increased EL intensity for this LEC.

3.3.1.1 Two charge carrier injection layers without ions

To confirm whether the previous LEC really operated as an LEC and not as an LED, the device was reproduced without the addition of the $LiCF_3SO_3$ ions. Aside from half-etching the ITO and spin coating the active layer only once, the device preparation was identical to the previous LEC.

The I-V curve measured for this device is shown in **Figure 3.3.1.1.1**.

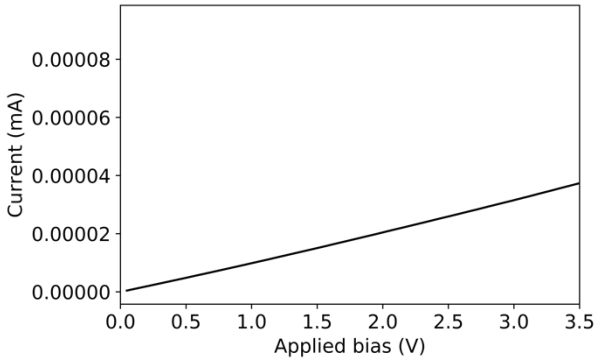

Figure 3.3.1.1.1 Linear sweep of a LEC with two charge carrier injection layers but without the addition of ions. Absolute currents are shown on the vertical axis since the emissive area could not be determined as the device did not emit light.

The I-V curve shows extremely low currents for the biases applied. More importantly, the device did not emit light. The barriers for charge carrier injection seem to be too high for current to flow in devices that do not incorporate ions. This experiment confirms that the device described in section **3.3.1 Two charge carrier injection layers** indeed operates as a LEC and not as a LED.

3.3.2 Device containing only a hole injection layer

Next, results of devices without an ETL are presented. Aside from spin coating 65 µL of master solution during the second spin, half-etching the ITO and depositing ±5,000 Å Al (and the absence of the electron injection layer), the device preparation was identical to the LEC described in section **3.3.1 Two charge carrier injection layers**.
The I-V curve measured for this device is shown in **Figure 3.3.2.1**.

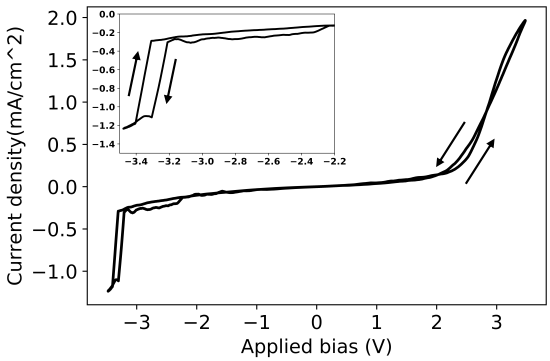

Figure 3.3.2.1. I-V curve of a LEC with one charge carrier injection layer. The curve was recorded through CV. The inset shows an amplification of the -3.5V - -2.2V range. The arrows to indicate the forward and the backward part of the scan are only shown in the inset for clarity.

The I-V curve shows diode-like behavior, under positive bias the current densities measured are higher than under negative bias. Also, the device emits light under positive bias while it does not under negative bias. The final stage of the curve under negative bias shows a rapid and linear increase in the current density. Since the current density increases at an oddly high applied bias voltage upon comparison with the positive scan and increases in a linear way, I hypothesize that the last data points under negative bias are inaccurate and off-trend, invigorating the diode-like behavior.
The scan shows reversible charging of the LEC, since the current densities on the way forward are almost equal to the current densities when going back to 0V, both for positive and for negative bias.
The measured current density at positive bias is around thirty times as low when compared with the LEC with two charge carrier injection layers. Since the EL intensity was not recorded for this device, no fair comparison on efficiency can be made between this LEC and the one with two charge carrier injection layers.
The three characteristic domains of an I-V curve are absent in the curve. Although the I-V curve shown only uses a scan window of ±3.5V, a different experiment revealed that this type of LEC can withstand applied biases of at least ±4V.
At larger applied biases than ±4V, the EL intensity starts to drop, and the current density does so, too. The latter phenomenon is visible in **Figure 3.3.2.2**.

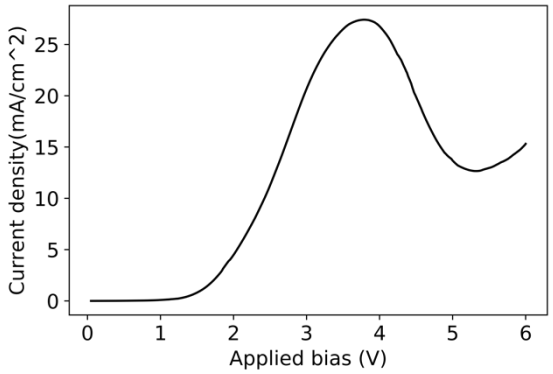

Figure 3.3.2.2. Linear sweep of a LEC with one charge carrier injection layer. The device fabrication was identical to the one described in section **3.3.1 Two charge carrier injection layers** except for the fact that three active layers were spin coated.

It remains uncertain what exactly happens within the LEC at applied biases larger than ~4V that causes the current density and EL intensity to drop. One explanation could be electrochemical degradation of the QDs in the active layer. The observations indicate that the electrochemical stability of this LEC is inferior to the electrochemical stability of the LEC with two charge carrier injection layers. The ZnO ETL could reduce the strength of the potential energy drop at the interface of the active layer (recall section **1.1.6 Semiconductor-metal contacts**), which in turn leads to better electrochemical stability.
Photographs of this LEC at different bias voltages during the linear sweep at forward bias are shown in **Figure 3.3.2.3**.

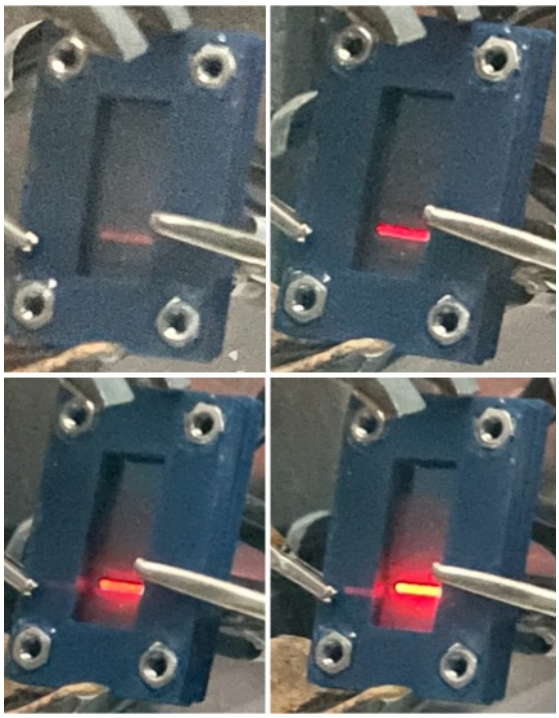

Figure 3.3.2.3. Photographs of a LEC with one charge carrier injection layer under operation. (*top left*) at ~2.5V. (*top right*) at ~3V. (*bottom left*) at ~4V. (*bottom right*) at ~5V.

The photographs show that the intensity of the EL increases as the applied bias is increased. This agrees with the finding on the EL of the LEC with two charge carrier injection layers. The photographs also show that the turn-on voltage of this LEC lies somewhere below 2.5V. The picture at the bottom right position was recorded at ~5V, whilst earlier the claim was made that the electrochemical stability is limited to only ~4V for this LEC. This contradiction very well shows that the results gathered differ for each fabricated LEC, even if LECs were produced in the same manner.

3.3.3 Zero charge carrier injection layers

Finally, the results of devices without any additional injection layers are presented.

Aside from depositing ±5,000 Å Al (and the absence of the two charge carrier injection layers), the device preparation was identical to the LEC described in section **3.3.1 Two charge carrier injection layers**.
The I-V curve measured for this device is shown in **Figure 3.3.3.1**.

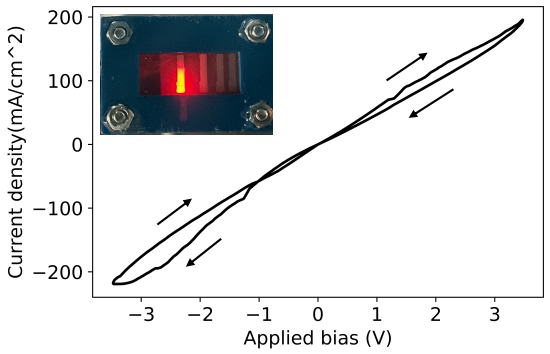

Figure 3.3.3.1. I-V curve of a three-layered, purely QD-based LEC. The curve is obtained through CV. The arrows indicate the forward and the backward part of the scan. The inset shows a photograph of the device under operation at forward bias.

The I-V curve shows nearly symmetrical behavior when considering the current density. The small difference in absolute currents at positive and negative bias might be caused by the fact that dissimilar electrodes were used. The symmetry of the current density was not observed in the EL, however. At -3.5V the LEC did not emit light, while it did at positive applied bias. This observation could possibly also be attributed to the use of unalike electrodes since this is the only difference in the LEC buildup upon reversing the applied bias.
The three characteristic domains of an I-V curve are absent in the curve. It could be the case that a larger scan window needs to be applied to see the three domains. However, the limited stability of the LEC discussed in section **3.3.2 Device containing only a hole injection layer** indicates that the three-layered LEC might not survive this scan window.
The current densities measured are high compared to the current densities of the other two LECs presented earlier. Next to this, the curve has a rather linear shape, and the current density increases at low applied potentials, two features that are not expected in a typical LEC I-V curve. An explanation for this could be the presence of a parasitic pinhole current. It could be the case that the Al and ITO are in direct contact at some places due to a non-homogeneous distribution of the active layer. This could lead to a parasitic background current between the Al and ITO without the charge carriers passing through the active layer, next to the current caused by electrons and holes traveling through the QD film (the photocurrent). If the total area of the pinholes is small, the current running through them is rather small too, resulting in a linear I-V curve with a small slope. It could be the case that this ohmic background current dominates the total current density, altering the shape of the I-V curve. Because the photocurrent is inferior to the current caused by the pinholes, but non-zero, light can still be emitted. If this scenario holds true, the typical I-V curve may be discovered through better active layer preparation and thereby avoiding pinholes. The two LECs with charge carrier injection layers did (better) show typical I-V curves. It could be the case that the supplementary layers prevent the pinholes from forming in these devices.
The development of the EL intensity as a function of the applied bias voltage is shown in **Figure 3.3.3.2**.

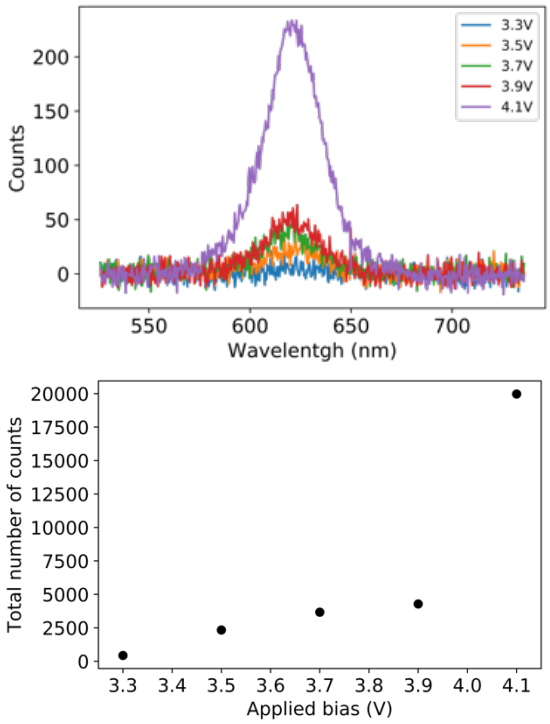

Figure 3.3.3.2. (*top*) Development of the EL intensity as the applied bias voltage is increased. (*bottom*) The integral of the peak of the EL intensity plotted versus the applied bias voltage.

The figure shows that the intensity of the EL increases as the applied bias voltage is increased. The increase in EL intensity becomes more pronounced at higher applied bias voltage. The peak of the EL intensity at 4.1V lies at 621 nm. This is a blueshift of 2 nm compared to the peak of the PL spectrum of the QDs in solution. The peak of the EL intensity has a HWHM of 17 nm, which is an increase of 1 nm compared to the HWHM of the peak of the PL spectrum of the QDs in

solution. It can be concluded that there is hardly any difference between the EL of this LEC and the PL of the QDs in solution. This agrees with the findings on the EL of the LEC with two charge carrier injection layers. The EL intensity was also measured at an applied bias of 4.3V. This measurement did not result in any signal, indicating that the device had degraded and that the electrochemical stability of this LEC is inferior to the LEC with two charge carrier injection layers but comparable to the LEC that only contained a HTL. The graphs also show that the turn-on voltage of the three-layered LEC lies somewhere around 3.3V, which is higher than the LEC that only contained a HTL but comparable to the LEC with two charge carrier injection layers.

If the total number of counts collected during an EL measurement are divided by the stable current density that runs through the LEC at a constant applied bias voltage, a sort of efficiency can be determined. Although the EQE of the device remains unknown, this number can be used to compare the devices made in this thesis to each other. Doing this for the three-layered LEC (where the data at 4V is taken to be the average between the data points at 3.9V and 4.1V) results in values of 15.99 and 82.23 at 3.5V and 4V, respectively. For the LEC containing two charge carrier injection layers, values of 20.45 and 62.81 are found at 3.5V and 4V, respectively. The two datasets indicate that these two LECs show comparable efficiencies at 3.5V and 4V. It seems that the additional charge carrier injection layers do not beneficially influence the efficiency of this LEC at these applied potentials and could therefore be totally unnecessary for this purpose.
Comparing the efficiency of the three-layered LEC to the LEC with only a HTL fairly is hard since the data collected for the two LECs is dissimilar. Next to this, it is found that the data that can be gathered for a LEC differs per measurement, even when LECs are fabricated in the exact same fashion. What can be said is that the measured current densities for the three-layered LEC are about a hundred times higher than the LEC with only a hole injection layer and roughly three times as high as the current densities measured for the LEC containing two charge carrier injection layers. I hypothesize that the remarkably higher current densities measured for the three-layered LEC are mainly caused by the parasitic pinhole current.

As stated in the introduction of this thesis, device fabrication of three-layered, purely QD-based LECs has been unsuccessful in research until now. Therefore, the device performance of this three-layered, purely QD-based LEC is the best to date. I believe that the prosperous device fabrication and operation of the three-layered, purely QD-based LEC shown above is mainly attributed to the LE. The LE makes the QDs soluble in polar solvents, which benefits the preparation of the master solution used for the active layer since PEO and $LiCF_3SO_3$ are also well soluble in this solvent. Next to this, the polar master solution sticks to the ITO very well after the ozone treatment. Most importantly, the QDs are expected to become more conductive since they are freed from their isolating hydrocarbon ligands. This could help both with the injection as well as transport of electrons and holes in the QD film.

4 Future research

The three LECs produced in this thesis could be compared to each other in a more systematic fashion. First, the devices need to be constructed in the exact same manner. Then, the exact same measurements need to be conducted on them. In particular, I-V curves through CVs could be gathered for the same scan window, turn-on voltages and turn-on times could be determined, lifetimes could be measured, EL spectra and intensity could be recorded as a function of applied bias and compared to the current density development and EQEs could be determined. In this way, the device performance of the three devices can be compared to each other and to literature accurately. These measurements might also give more insight into the influence of the charge carrier injection layers.

The conductivity enhancement of the QD film after LE has not been confirmed in this thesis. The conductivity of QD films before and after LE could be measured and might give insights into why the three-layered LEC could be operated successfully in this thesis.

Lastly, the performance of the LECs in this thesis will be inferior to the performance of (QD-based) LEDs. For the LECs to become competitive to these LEDs, their performance must be improved. Only in this way may the large-scale diffusion for LECs outpace the one for LEDs.[12]

One way to improve the performance of the LECs of this thesis can be found in boosting the PLQY of the QDs. The LECs in this thesis were produced with QDs with a PLQY of only 22%. If their PLQY can near unity, the EL intensity can already improve almost fivefold. Therefore, a different LE can be investigated that does not lower the PLQY as significantly. Alternatively, QD synthesis routes can be explored that do not incorporate long, isolating hydrocarbon ligands. If the QD surface can be covered by short (and polar) ligands, the QDs might already be soluble in polar solvents and have enhanced conductivity. A LE might not even be needed in this case, possibly resulting in QDs with a heightened PLQY.

If the QDs could be produced using alternative materials, i.e. InP, the toxicity problems related to CdSe can also be circumvented.[84]

Another factor that lowers the performance of LECs is the formation of black spots, which reduce the emissive area. Black spot formation has been reported for polymer-based and iTMC-based LECs,[68, 85, 86] and was also observed sometimes in the LECs described in this thesis.

The black spots commonly arise when the LEC is under operation. However, literature shows that part of the black spots disappear again if the applied bias is switched off. Researchers therefore hypothesize that black spot formation is the result of regions of heavy doping. It was also shown in literature that deposition of the Al cathode can lead to black spot formation, even when the device is not under operation. The exact origin of black spot formation is thus unrevealed to date. It is therefore hard to come up with solutions for this phenomenon.

The partial disappearance of black spots after relaxation of the LEC shows that deterioration of LEC performance cannot be fully accredited to irreversible side reactions. However, part of it can be and one explanation could be a side reaction with the ion carriage material PEO.[87] In LECs based on MEH-PPV, the reduction potential of PEO lies below the conduction band of MEH-PPV. Injection of electrons into the LEC could therefore reduce the PEO, as opposed to filling the conduction band of MEH-PPV. The first process is energetically more favorable, while the latter is kinetically more favorable due to the insulating nature of PEO.[49] Therefore, both processes are expected to happen in this type of LEC. The reduction of PEO happens mostly at the cathode interface, hampering the electron injection into the LEC and misbalancing the charge carrier injection rates.

The energy levels of the valence band and conduction band of the QDs used in this thesis were not investigated. However, it could be that the reduction of PEO also happens in the LECs discussed in this thesis. The PEO could therefore affect the performance of these LECs. Performance improvement could possibly be established by finding QDs that have a conduction band that lies lower in energy or by investigating ion transport materials that have a higher reduction potential.

Finally, performance could be enhanced by improving the device fabrication procedures. Examples of possible targets for optimization are the active layer composition, thickness, and drying process. Different electrode materials could also be investigated to for instance better balance the charge carrier injection rates. In addition to this, the p-n junction could be fixed by making use of a high melting point electrolyte.[38] Upon cooling the devices from an elevated temperature to room temperature while the device is under operation, the doping might not relax to its intrinsic state and yield a permanent p-n

junction. In this way, the doping is long-lasting, and this might greatly improve features like the turn-on time.

5. Conclusion

Three types of purely CdSe/CdS/ZnS-based LECs were produced and operated: one with two charge carrier injection layers, one with one charge carrier injection layer and one without the use of charge carrier injection layers. Maximum current densities were found to decrease as the charge carrier injection layers are removed. For the three-layered LEC, however, current densities were found to be highest, probably because of a parasitic pinhole current. The current density was found to be nearly symmetrical for the three-layered LEC, while the other two LECs showed diode-like behavior. All LECs emitted light at positive bias while they did not at negative bias. The intensity of the EL has been confirmed to increase as the applied bias voltage is increased for all the LECs. The three-layered, four-layered, and five-layered LECs had turn-on voltages of approximately 3.3V, 2.5V and 3 - 3.5V, respectively, and could be operated safely until around 4.1V, 4V and 8V, respectively. It has been confirmed that the devices operate as LECs and not as LEDs. The efficiencies of the three-layered and five-layered LEC seem to be comparable.

The successful device operation of the (three-layered) LEC(s) is attributed to the LE carried out on the QDs used as luminophore. Analysis showed that the native, isolating hydrocarbon ligands can be stripped from the surface almost completely and can be replaced by short BF_4^- anions that bind to the surface weakly. This treatment is expected to enhance the conductivity of the QD films significantly but decreases the PLQY from 86% to 22%.

In the Introduction to this thesis, the hypothesis was put forward that the simple, three-layered device structure of a LEC should be able to be constructed with any luminophore. The results of the three-layered, purely QD-based LEC in this thesis suggest that this hypothesis might very well be true. This result will hopefully increase the scientific interest in the field of LECs and might consequently lead to rapid improvement of their performance.

References

1. Gandate, C.; Parauha, Y. R.; Mushtaque, S. G. M.; Dhoble, S. J., Current progress and comparative study of performance of the energy saving lighting devices: a review. *Journal of Physics: Conference Series* **2021,** *1913* (1).

2. Ayres, R. U., The History of Artificial Light. In *The History and Future of Technology: Can Technology Save Humanity from Extinction?*, Springer International Publishing: Cham, 2021; pp 339-364.

3. Zissis, G.; Bertoldi, P.; Serrenho, T. *Update on the Status of LED-Lighting world market since 2018*; EUR 30500 EN; Publications Office of the European Union, Luxembourg: 2021.

4. Li, Y.; Gao, J.; Yu, G.; Cao, Y.; Heeger, A. J., ac impedance of polymer light-emitting electrochemical cells and light-emitting diodes: a comparative study. *Chemical Physics Letters* **1998,** *287* (1-2), 83-88.

5. Kido, J.; Kimura, M.; Nagai, K., Multilayer white light-emitting organic electroluminescent device. *Science* **1995,** *267* (5202), 1332-4.

6. Passannante, A., An examination of improvements in OLED quality and fabrication. *University of Washington* **2020,** *1*.

7. Kang, J.; Cho, Y.; Jang, W., Long-Term Reliability Characteristics of OLED Panel and Luminaires for General Lighting Applications. *Applied Sciences* **2020,** *11* (1).

8. LED, C. https://cree-led.com/products/xlamp-leds-discrete (accessed 7 Octobre).

9. Halper, M., Philips turbocharges the LED bulb, claiming huge efficiency breakthrough with Dubai. *LEDs Magazine* October 5, 2016.

10. Wang, B.-K.; Lee, W.-K.; Lin, K.-C.; Chen, P.-J.; Huang, Y.-H.; Wen, S.-W.; Zeng, X.; Ni, F.; Gong, S.; Yang, C.; Wu, C.-C., Realization of exceeding 80% external quantum efficiency in organic light-emitting diodes using high-index substrates and highly horizontal emitters. *Organic Electronics* **2021,** *89*.

11. Bauri, J.; Choudhary, R. B.; Mandal, G., Recent advances in efficient emissive materials-based OLED applications: a review. *Journal of Materials Science* **2021**.

12. Ortt, J. R.; Schoormans, J. P. L., The pattern of development and diffusion of breakthrough communication technologies. *European Journal of Innovation Management* **2004,** *7* (4), 292-302.

13. Pei, Q.; Yu, G.; Zhang, C.; Yang, Y.; Heeger, A. J., Polymer light-emitting electrochemical cells. *Science* **1995,** *269* (5227), 1086-8.

14. Martinez-Alonso, M.; Cerda, J.; Momblona, C.; Pertegas, A.; Junquera-Hernandez, J. M.; Heras, A.; Rodriguez, A. M.; Espino, G.; Bolink, H.; Orti, E., Highly Stable and Efficient Light-Emitting Electrochemical Cells Based on Cationic Iridium Complexes Bearing Arylazole Ancillary Ligands. *Inorg Chem* **2017,** *56* (17), 10298-10310.

15. Chen, Y.-Z.; Luo, D.; Hsiang, C.-H.; Yi, R.-H.; Lin, C.-H.; Lu, C.-W.; Liu, S.-W.; Chang, C.-H.; Su, H.-C., Highly efficient blue and white light-emitting electrochemical cells employing substrates containing embedded diffusive layers. *Organic Electronics* **2020,** *77*.

16. Sun, Q.; Li, Y.; Pei, Q., Polymer Light-Emitting Electrochemical Cells for High-Efficiency Low-Voltage Electroluminescent Devices. *J. Display Technol.* **2007,** *3* (2), 211-224.

17. Yang, C.; Sun, Q.; Qiao, J.; Li, Y., Ionic Liquid Doped Polymer Light-Emitting Electrochemical Cells. *The Journal of Physical Chemistry B* **2003,** *107* (47), 12981-12988.

18. Costa, R. D.; Orti, E.; Bolink, H. J.; Monti, F.; Accorsi, G.; Armaroli, N., Luminescent ionic transition-metal complexes for light-emitting electrochemical cells. *Angew Chem Int Ed Engl* **2012,** *51* (33), 8178-211.

19. Slinker, J. D.; Rivnay, J.; Moskowitz, J. S.; Parker, J. B.; Bernhard, S.; Abruña, H. D.; Malliaras, G. G., Electroluminescent devices from ionic transition metal complexes. *J. Mater. Chem.* **2007,** *17* (29), 2976-2988.

20. Su, H. C.; Hsu, J. H., Improving the carrier balance of light-emitting electrochemical cells based on ionic transition metal complexes. *Dalton Trans* **2015,** *44* (18), 8330-45.

21. Park, S.; Yang, J.; Kim, S.; Hahm, D.; Jo, H.; Bae, W. K.; Kang, M. S., Light-Emitting Electrochemical Cells with Polymer-Blended InP/ZnSeS Quantum Dot Active Layer. *Advanced Optical Materials* **2020,** *8* (24).

22. Frohleiks, J.; Wepfer, S.; Kelestemur, Y.; Demir, H. V.; Bacher, G.; Nannen, E., Quantum Dot/Light-Emitting Electrochemical Cell Hybrid Device and Mechanism of Its Operation. *ACS Appl Mater Interfaces* **2016,** *8* (37), 24692-8.

23. Chiu, Y.-C.; Yi, R.-H.; Ou, T.-Y.; Luo, D.; Lien, J.-Y.; Yang, Z.-P.; Lu, C.-W.; Su, H.-C., Optimizing carrier balance of a red quantum-dot light-emitting electrochemical cell with a carrier injection layer of cationic Ir(III) complex. *Organic Electronics* **2021,** *88*.

24. Nannen, E.; Frohleiks, J.; Gellner, S., Light-Emitting Electrochemical Cells Based on Color-Tunable Inorganic Colloidal Quantum Dots. *Advanced Functional Materials* **2020,** *30* (33).

25. Qian, G.; Lin, Y.; Wantz, G.; Davis, A. R.; Carter, K. R.; Watkins, J. J., Saturated and Multi-Colored Electroluminescence from Quantum Dots Based Light Emitting Electrochemical Cells. *Advanced Functional Materials* **2014,** *24* (28), 4484-4490.

26. Bader, A. J.; Ilkevich, A. A.; Kosilkin, I. V.; Leger, J. M., Precise color tuning via hybrid light-emitting electrochemical cells. *Nano Lett* **2011,** *11* (2), 461-5.

27. Seitz, F.; Johnson, R. P., Modern Theory of Solids. I. *Journal of Applied Physics* **1937,** *8* (2), 84-97.

28. Li, S. S., *Semiconductor Physical Electronics second edition*. Springer: 2006.

29. Nebel, C. E., Semiconductor materials: From gemstone to semiconductor. *Nat Mater* **2003,** *2* (7), 431-2.

30. Polese, J. M., Electron-Hole Recombination. **2021**.

31. Woodyard, J. R. Nonlinear circuit device utilizing germanium. 1950.

32. Smith, D. L., Steady state model for polymer light-emitting electrochemical cells. *Journal of Applied Physics* **1997,** *81* (6), 2869-2880.

33. TheNoise p-n junction. https://en.wikipedia.org/wiki/P–n_junction (accessed January 3).

34. Dukovic, G. Particle in a box: quantum dots, developed by Gordana Dukovic and Kyle Schnitzenbaumer. https://www.colorado.edu/lab/dukovicgroup/sites/default/files/attached-files/particle_in_a_box_website.pdf (accessed november 9).

35. Park, J.; Joo, J.; Kwon, S. G.; Jang, Y.; Hyeon, T., Synthesis of monodisperse spherical nanocrystals. *Angew Chem Int Ed Engl* **2007,** *46* (25), 4630-60.

36. Wood, V.; Bulovic, V., Colloidal quantum dot light-emitting devices. *Nano Rev* **2010,** *1*.

37. Shirasaki, Y.; Supran, G. J.; Bawendi, M. G.; Bulović, V., Emergence of colloidal quantum-dot light-emitting technologies. *Nature Photonics* **2012,** *7* (1), 13-23.

38. Gudjonsdottir, S.; van der Stam, W.; Koopman, C.; Kwakkenbos, B.; Evers, W. H.; Houtepen, A. J., On the Stability of Permanent Electrochemical Doping of Quantum Dot, Fullerene, and Conductive Polymer Films in Frozen Electrolytes for Use in Semiconductor Devices. *ACS Appl Nano Mater* **2019,** *2* (8), 4900-4909.

39. Hines, M. A.; Guyot-Sionnest, P., Synthesis and Characterization of Strongly Luminescing ZnS-Capped CdSe Nanocrystals. *The Journal of Physical Chemistry* **1996,** *100* (2), 468-471.

40. Lifshitz, E.; Brumer, M.; Kigel, A.; Sashchiuk, A.; Bashouti, M.; Sirota, M.; Galun, E.; Burshtein, Z.; Le Quang, A. Q.; Ledoux-Rak, I.; Zyss, J., Air-stable PbSe/PbS and PbSe/PbSexS1-x core-shell nanocrystal quantum dots and their applications. *J Phys Chem B* **2006,** *110* (50), 25356-65.

41. Park, Y. S.; Malko, A. V.; Vela, J.; Chen, Y.; Ghosh, Y.; Garcia-Santamaria, F.; Hollingsworth, J. A.; Klimov, V. I.; Htoon, H., Near-unity quantum yields of biexciton emission from CdSe/CdS nanocrystals measured using single-particle spectroscopy. *Phys Rev Lett* **2011,** *106* (18), 187401.

42. Mocatta, D.; Cohen, G.; Schattner, J.; Millo, O.; Rabani, E.; Banin, U., Heavily doped semiconductor nanocrystal quantum dots. *Science* **2011,** *332* (6025), 77-81.

43. Koh, W. K.; Koposov, A. Y.; Stewart, J. T.; Pal, B. N.; Robel, I.; Pietryga, J. M.; Klimov, V. I., Heavily doped n-type PbSe and PbS nanocrystals using ground-state charge transfer from cobaltocene. *Sci Rep* **2013,** *3*, 2004.

44. Shim, M.; Guyot-Sionnest, P., n-type colloidal semiconductor nanocrystals. *Nature* **2000,** *407* (6807), 981-3.

45. Rinehart, J. D.; Schimpf, A. M.; Weaver, A. L.; Cohn, A. W.; Gamelin, D. R., Photochemical electronic doping of colloidal CdSe nanocrystals. *J Am Chem Soc* **2013,** *135* (50), 18782-5.

46. Schimpf, A. M.; Gunthardt, C. E.; Rinehart, J. D.; Mayer, J. M.; Gamelin, D. R., Controlling carrier densities in photochemically reduced colloidal ZnO nanocrystals: size dependence and role of the hole quencher. *J Am Chem Soc* **2013,** *135* (44), 16569-77.

47. Guyot-Sionnest, P., Charging colloidal quantum dots by electrochemistry. *Microchimica Acta* **2008,** *160* (3), 309-314.

48. Gudjonsdottir, S.; Van Der Stam, W.; Koopman, C.; Kwakkenbos, B.; Evers, W. H.; Houtepen, A. J., On the Stability of Permanent Electrochemical Doping of Quantum Dot, Fullerene, and Conductive Polymer Films in Frozen Electrolytes for Use in Semiconductor Devices. *ACS applied nano materials* **2019,** *2* (8), 4900-4909.

49. van Reenen, S.; Kemerink, M., Light-Emitting Electrochemical Cells:
Mechanisms and Formal Description. In *Light-Emitting Electrochemical Cells: Concepts, Advances and Challenges*, Costa, R. D., Ed. Springer International Publishing: Cham, 2017; pp 3-45.

50. Zvaigzne, M.; Alexandrov, A.; Tkach, A.; Lypenko, D.; Nabiev, I.; Samokhvalov, P., Optimizing the PMMA Electron-Blocking Layer of Quantum Dot Light-Emitting Diodes. *Nanomaterials (Basel)* **2021,** *11* (8).

51. Caruge, J. M.; Halpert, J. E.; Wood, V.; Bulović, V.; Bawendi, M. G., Colloidal quantum-dot light-emitting diodes with metal-oxide charge transport layers. *Nature Photonics* **2008,** *2* (4), 247-250.

52. Song, S.-H.; Yoo, J.-I.; Kim, H.-B.; Kim, Y.-S.; Soo Kim, S.; Song, J.-K., Hole injection improvement in quantum-dot light-emitting diodes using bi-layered hole injection layer of PEDOT:PSS and V2O. *Optics & Laser Technology* **2022,** *149*.

53. Terada, S.; Ueda, H.; Ono, T.; Saitow, K.-i., Orange–Red Si Quantum Dot LEDs from Recycled Rice Husks. *ACS Sustainable Chemistry & Engineering* **2022,** *10* (5), 1765-1776.

54. Yoo, J.-Y.; Jung, W. H.; Lee, C. W.; Chin, B. D.; Kim, J.-G.; Kim, J. S., Enhanced device performance of quantum-dot light-emitting diodes via 2,2′-Bipyridyl ligand exchange. *Organic Electronics* **2021,** *99*.

55. Guyot-Sionnest, P., Colloidal quantum dots. *Comptes Rendus Physique* **2008,** *9* (8), 777-787.

56. Yu, D.; Wang, C.; Guyot-Sionnest, P., n-Type conducting CdSe nanocrystal solids. *Science* **2003,** *300* (5623), 1277-80.

57. Gao, Y.; Aerts, M.; Sandeep, C. S.; Talgorn, E.; Savenije, T. J.; Kinge, S.; Siebbeles, L. D.; Houtepen, A. J., Photoconductivity of PbSe quantum-dot solids: dependence on ligand anchor group and length. *ACS Nano* **2012,** *6* (11), 9606-14.

58. Guyot-Sionnest, P.; Wang, C., Fast Voltammetric and Electrochromic Response of Semiconductor Nanocrystal Thin Films. *The Journal of Physical Chemistry B* **2003,** *107* (30), 7355-7359.

59. Wang, Z.; Hu, Z.; Kamarudin, M. A.; Kapil, G.; Tripathi, A.; Shen, Q.; Yoshino, K.; Minemoto, T.; Pandey, S. S.; Hayase, S., Enhancement of charge transport in quantum dots solar cells by N-butylamine-assisted sulfur-crosslinking of PbS quantum dots. *Solar Energy* **2018,** *174*, 399-408.

60. deMello, J. C.; Tessler, N.; Graham, S. C.; Friend, R. H., Ionic space-charge effects in polymer light-emitting diodes. *Physical Review B* **1998,** *57* (20), 12951-12963.

61. deMello, J. C., Interfacial feedback dynamics in polymer light-emitting electrochemical cells. *Physical Review B* **2002,** *66* (23).

62. Hoven, C. V.; Wang, H.; Elbing, M.; Garner, L.; Winkelhaus, D.; Bazan, G. C., Chemically fixed p-n heterojunctions for polymer electronics by means of covalent B-F bond formation. *Nat Mater* **2010,** *9* (3), 249-52.

63. Matyba, P.; Maturova, K.; Kemerink, M.; Robinson, N. D.; Edman, L., The dynamic organic p-n junction. *Nat Mater* **2009,** *8* (8), 672-6.

64. van Reenen, S.; Matyba, P.; Dzwilewski, A.; Janssen, R. A.; Edman, L.; Kemerink, M., A unifying model for the operation of light-emitting electrochemical cells. *J Am Chem Soc* **2010,** *132* (39), 13776-81.

65. Manzanares, J. A.; Reiss, H.; Heeger, A. J., Polymer Light-Emitting Electrochemical Cells: A Theoretical Study of Junction Formation under Steady-State Conditions. *The Journal of Physical Chemistry B* **1998,** *102* (22), 4327-4336.

66. Gao, J.; Dane, J., Visualization of electrochemical doping and light-emitting junction formation in conjugated polymer films. *Applied Physics Letters* **2004,** *84* (15), 2778-2780.

67. van Reenen, S.; Janssen, R. A. J.; Kemerink, M., Fundamental Tradeoff between Emission Intensity and Efficiency in Light-Emitting Electrochemical Cells. *Advanced Functional Materials* **2015,** *25* (20), 3066-3073.

68. Slinker, J.; Bernards, D.; Houston, P. L.; Abruna, H. D.; Bernhard, S.; Malliaras, G. G., Solid-state electroluminescent devices based on transition metal complexes. *Chem Commun (Camb)* **2003,** (19), 2392-9.

69. King, S. M.; Dai, D.; Rothe, C.; Monkman, A. P., Exciton annihilation in a polyfluorene: Low threshold for singlet-singlet annihilation and the absence of singlet-triplet annihilation. *Physical Review B* **2007,** *76* (8).

70. Qu, L.; Peng, Z. A.; Peng, X., Alternative Routes toward High Quality CdSe Nanocrystals. *Nano Letters* **2001,** *1* (6), 333-337.

71. Dong, A.; Ye, X.; Chen, J.; Kang, Y.; Gordon, T.; Kikkawa, J. M.; Murray, C. B., A generalized ligand-exchange strategy enabling sequential surface functionalization of colloidal nanocrystals. *J Am Chem Soc* **2011,** *133* (4), 998-1006.

72. Lim, J.; Park, M.; Bae, W. K.; Lee, D.; Lee, S.; Lee, C.; Char, K., Highly efficient cadmium-free quantum dot light-emitting diodes enabled by the direct formation of excitons within InP@ZnSeS quantum dots. *ACS Nano* **2013,** *7* (10), 9019-26.

73. Huang, J.; Miller, P. F.; de Mello, J. C.; de Mello, A. J.; Bradley, D. D. C., Influence of thermal treatment on the conductivity and morphology of PEDOT/PSS films. *Synthetic Metals* **2003,** *139* (3), 569-572.

74. Kim, Y.; Ballantyne, A.; Nelson, J.; Bradley, D., Effects of thickness and thermal annealing of the PEDOT:PSS layer on the performance of polymer solar cells. *Organic Electronics* **2009,** *10* (1), 205-209.

75. Fulmer, G. R.; Miller, A. J. M.; Sherden, N. H.; Gottlieb, H. E.; Nudelman, A.; Stoltz, B. M.; Bercaw, J. E.; Goldberg, K. I., NMR Chemical Shifts of Trace Impurities: Common Laboratory Solvents, Organics, and Gases in Deuterated Solvents Relevant to the Organometallic Chemist. *Organometallics* **2010,** *29* (9), 2176-2179.

76. Imran, M.; Ijaz, P.; Goldoni, L.; Maggioni, D.; Petralanda, U.; Prato, M.; Almeida, G.; Infante, I.; Manna, L., Simultaneous Cationic and Anionic Ligand Exchange For Colloidally Stable CsPbBr3 Nanocrystals. *ACS Energy Letters* **2019,** *4* (4), 819-824.

77. Jorapur, Y. R.; Mizoshita, N.; Maegawa, Y.; Nakagawa, H.; Hasegawa, T.; Tani, T.; Inagaki, S.; Shimada, T., A Novel Sol–Gel Approach to Highly Condensed Silicas at Low Temperature. *Chemistry Letters* **2012,** *41* (3), 280-281.

78. Brownstein, S., Complex fluoroanions in solution. VII. Replacement of fluoride by trifluoroacetate. *Canadian Journal of Chemistry* **1978,** *56* (3), 343-347.

79. Pu, Y. C.; Fan, H. C.; Chang, J. C.; Chen, Y. H.; Tseng, S. W., Effects of Interfacial Oxidative Layer Removal on Charge Carrier Recombination Dynamics in InP/ZnSexS1-x Core/Shell Quantum Dots. *J Phys Chem Lett* **2021,** *12* (30), 7194-7200.

80. Mićić, O. I.; Jones, K. M.; Cahill, A.; Nozik, A. J., Optical, Electronic, and Structural Properties of Uncoupled and Close-Packed Arrays of InP Quantum Dots. *The Journal of Physical Chemistry B* **1998,** *102* (49), 9791-9796.

81. Mićić, O. I.; Cheong, H. M.; Fu, H.; Zunger, A.; Sprague, J. R.; Mascarenhas, A.; Nozik, A. J., Size-Dependent Spectroscopy of InP Quantum Dots. *The Journal of Physical Chemistry B* **1997,** *101* (25), 4904-4912.

82. Mićić, O. I.; Sprague, J.; Lu, Z.; Nozik, A. J., Highly efficient band-edge emission from InP quantum dots. *Applied Physics Letters* **1996,** *68* (22), 3150-3152.

83. Frohleiks, J.; Gellner, S.; Wepfer, S.; Bacher, G.; Nannen, E., Design and Realization of White Quantum Dot Light-Emitting Electrochemical Cell Hybrid Devices. *ACS Appl Mater Interfaces* **2018,** *10* (49), 42637-42646.

84. (EU), C. D. D., 2015/863 of 31 March 2015 amending Annex II to Directive 2011/65/EU of the European Parliament and of the Council as regards the list of restricted substances. Official Journal of the European Union, 2015; p 3.

85. AlTal, F.; Gao, J., Long-term testing of polymer light-emitting electrochemical cells: Reversible doping and black spots. *Organic Electronics* **2015,** *18*, 1-7.

86. Fang, J.; Matyba, P.; Robinson, N. D.; Edman, L., Identifying and alleviating electrochemical side-reactions in light-emitting electrochemical cells. *J Am Chem Soc* **2008,** *130* (13), 4562-8.

87. Shin, J. H.; Xiao, S.; Edman, L., Polymer Light-Emitting Electrochemical Cells: The Formation and Effects of Doping-Induced Micro Shorts. *Advanced Functional Materials* **2006,** *16* (7), 949-956.